CHEMISTRY AND STRUCTURE OF Ru/SiO2 AND Ru/ Al_2O_3 INTERFACES

by

SAMEER SA'ADALLAH EZZAT

B.C. University of Mosul, 1998

M.Sc. University of Mosul, 2000

A dissertation submitted in partial fulfillment of the requirements

for the degree of Doctor of Philosophy

in the Department of Chemistry

in the College of Science

at the University of Central Florida

Orlando, Florida

Spring Term

2019

Major Professor: Andres Campiglia, Kevin R. Coffey

© 2019 SAMEER SA’ADALLAH EZZAT

ABSTRACT

The resistivity size effect in nanoscale metals is of both scientific and technological interest, the latter due to its importance to interconnects between transistors in integrated circuits. In this work we report the variation of resistivity associated with surface scattering of ex-situ annealed single crystal Ru thin films grown on sapphire substrates by sputter deposition. A set of samples were overcoated with dielectric and subjected to a variety of reducing and oxidizing anneals. The changes in the chemistry and structure of the dielectric interface induced by the anneals, as determined by x-ray reflectivity and x-ray photoelectron spectroscopy measurements, are related to the changes in the specularity of the surface for electron scattering in the context of the Fuchs-Sondheimer semi-classical model of the resistivity size effect.

This dissertation is dedicated to my father (1939-2005), my mother, and my wife. They have been a constant source of support and encouragement during the challenges of doctoral study and I am really thankful for having them in my life.

My lovely kids

Ibrahim, Estabraq, and Razan

For inspiring me to not give up.

My brothers and sister

For their love, endless support and encouragement.

ACKNOWLEDGMENTS

It is a milestone that would have not been possible without the continuous support and guidance of my research advisor, Professor Kevin R. Coffey, and my academic advisor, Professor Dr. Andres D. Campiglia. Their continuous and enormous support during my Ph.D. research with their patience, enthusiasm, and immense knowledge was greatly appreciated. Their guidance helped me through the duration of my Ph.D. experience and preparation of this dissertation.

I extend my thanks to the dissertation committee members Dr. James Harper, Dr. Shengli Zou, and Dr. Andrew Frazer.

I would like to thank the Iraqi government and Ministry of Higher Education and Scientific Research for providing this opportunity and their continuous support.

Edward Dein and Dr. Prabhu Doss Mani are important people, they had helped me in my research learning everything in clean room right from sputtering tools to lithography process.

I would like to thank Dr. William Kaden and Asim Khaniya for all help.

Special thanks to my brothers and sister, and do not forget my friends during my PhD studies.

My colleagues of Dr. Coffey's group

My sincere thanks to Kirk Scammon, Karen Glidewell, Mikhail Klimov, and Dr. Mike Hawkridge for assistance with characterization facilities

TABLE OF CONTENTS

ABSTRACT iii
ACKNOWLEDGMENTS v
TABLE OF CONTENTS vi
LIST OF FIGURES ix
LIST OF TABLES xiii
CHAPTER 1 INTRODUCTION 1
1.1 Ruthenium 1
1.2 Ruthenium oxidation 3
1.3 Reduction of RuO_2 (110) on Ru (0001) surface 8
1.3.1 Reduction by hydrogen 8
1.3.2 Reduction by carbon monoxide 9
1.3.3 Reduction by methanol 10
CHAPTER 2 BACKGROUND AND MOTIVATION 11
2.1 Resistivity of thin metal films 11
2.2 Adsorbate induced changes in resistivity of atomically clean metal films 12
2.2.1 Suhrmann model 13
2.2.2 Sachtler model 15
2.2.3 Fuchs-Sondheimer model 15
2.2.4 The scattering hypothesis 16
2.3 Resistivity due to variation of metal film thickness 19
CHAPTER 3 EXPERIMENTAL 24
3.1 Introduction 24
3.2 Sputter deposition 24
3.3 XRD and XRR characterization 27
3.3.1 XRD characterization 27
3.3.2 XRR characterization 27
3.4 Four-Point Resistivity Measurement 28
3.5 Sample preparation details 30
3.5.1 Ru single crystal film deposition 30
3.5.2 Anneal to 700°C 32

3.5.3 Step anneal to 950°C 34
3.5.4 Additional anneals for series 3 34
3.5.5 SiO_2 overlayer depositions 35
3.5.6 Al_2O_3 overlayer depositions 36
3.5.7 Additional anneals for series 5 36
3.5.8 Additional anneals for series 6 38
CHAPTER 4 SINGLE CRYSTAL RUTHENIUM FILMS 39
4.1 X-ray diffraction 39
4.2 X-ray reflectivity 41
4.3 Roughness sample series one 42
4.4 Modelling 43
4.5 Resistivity 44
4.5.1 Resistivity sample series 1 44
4.5.2 Resistivity sample series 2 and 3 45
4.5.3 Sample series 3 47
4.6 LEED characterization 48
4.7 XPS characterization Ru 50
CHAPTER 5 Ru/SiO_2 and Ru/Al_2O_3 INTERFACE 54
5.1 XRR layer thickness 54
5.2 XPS characterization Ru/SiO_2 55
5.3 LEED of Ru/SiO_2 and Ru/Al_2O_3 58
5.4 Resistivity and specularity 59
5.4.1 Sample series 4 - evaporated SiO_2 on Ru 20 nm films 59
5.4.2 Sample series 5 - sputtered SiO_2 on Ru 20 nm films 60
5.4.3 Samples series 6 - Sputtered Al_2O_3 on Ru 20 nm films 65
CHAPTER 6 RUTHENIUM ON $(11\bar{2}0)$, $(10\bar{1}0)$, $(10\bar{1}2)$, and $(10\bar{1}4)$ SAPPHIRE 68
6.1 Introduction 68
6.2 Ru on sapphire $(11\bar{2}0)$ 69
6.3 Ru on sapphire $(10\bar{1}0)$ 73
6.4 Ru on sapphire $(10\bar{1}2)$ 75
6.5 Ru on sapphire $(10\bar{1}4)$ 76
6.6 Conclusion 78

CHAPTER 7 SUMMARY 79
CHAPTER 8 CHAPTER 8 FUTURE WORK 81
8.1 Deposit Ru thin film on sapphire ($11\bar{2}0$) and sapphire ($10\bar{1}0$) 81
8.2 Ru (0001)/Metal oxide interfaces 81
8.3 The effect of annealing temperature 82
LIST OF REFERENCES 83

LIST OF FIGURES

Figure 1-1 The hcp crystal structure with ABA stacking. 1

Figure 1-2 The hcp crystal structure, (a) identifies the basal plane as the (0001) plane and is the plane containing the darkened circles. Figure 1.2 (a) also identifies the [0001] direction by the arrow that is perpendicular to the (0001) plane. Figure 1.2 (b) similarly identifies the $(11\bar{2}0)$ plane and $[11\bar{2}0]$ direction while Figure 1.2 (c) identifies an $(10\bar{1}0)$ plane and $[10\bar{1}0]$ direction . 2

Figure 1-3 STM images show the chemisorbed oxygen on Ru (0001) 5

Figure 1-4 Calculated free energy O-Ru (0001) structures 6

Figure 1-5 The RuO_2 (110) and RuO_2 (100) on Ru (0001) substrate. 7

Figure 1-6 Surface X-ray diffraction explain the reduction of RuO_2 on Ru (0001) surface via H_2 molecules at various temperatures. 9

Figure 2-1 Resistivity increased due to gas adsorption on a thin film conductor 13

Figure 2-2 Four theories that have been proposed to understand the resistivity change due to molecules or atoms absorbing on the surface of a thin film. 14

Figure 2-3 The resistivity effect of O_2, CO, and C_2H_4 adsorption on Ag thin films 17

Figure 2-4 Various adsorbates on Ru (0001) 18

Figure 2-5 SiO2 on Ru (0001), (a) O-poor (b) O-rich 21

Figure 2-6 (a) Atomic structure of an ideal double-layer silicatene on Ru (0001). (b) STM image of crystalline and amorphous structures of the silicatene. 22

Figure 3-1 Geometry of sputtering deposition.. 26

Figure 3-2 Representative XRR data from a 4.6nm thick SiO_2 on a 20.8nm-thick Ru (0001) layer. (a) upper (black) curve is for measured data shifted by a factor of 10^1 for clarity and (b) the lower (red) curve is for fitted mpdel. 28

Figure 3-3 Diagram of the Van der Pauw geometry dipping probe 29

Figure 4-1 The diagram of (a) theta-2theta scan and (b) phi scan 39

Figure 4-2 Specular XRD scan for a Ru film on sapphire (0001) deposited at 700ºC with thickness d = 39.8 nm 40

Figure 4-3 XRD ϕ scan of the Ru $\{11\bar{2}2\}$ peaks overlaid with a scan of the sapphire $\{11\bar{2}6\}$ peaks 41

Figure 4-4 XRR data from 40 nm-thick Ru (0001) layer deposited at 400°C. (a) upper (red) curve is Ru after annealed and shifted by a factor of 10 for clarity and (b) the lower (blue) curve is Ru before as deposited. 42

Figure 4-5 Ru roughness of Ru thin films, as deposited and after annealed. 43

Figure 4-6 Resistivity of Ru thin films as deposited and after annealed at 700°C. 45

Figure 4-7 Resistivity versus thickness for c-axis single crystal Ru films deposited at 350°C (circles) and 700°C (squares) and ex-situ step-annealed to 950°C in Ar/H_2 3%. The solid line is the calculation of the FS model. 46

Figure 4-8 Resistivity of Ru 20 nm thin film during the annealing process 47

Figure 4-9 LEED images at 68 eV for an air exposed Ru film (a) after deposition at 350°C, (b) after deposition at 700°C, (c) after deposition at 700°C and ex-situ annealing to 950°C in Ar/3%H_2, and (d) a sample Ar ion beam cleaned and annealed to 1,000°C in UHV conditions with an H_2 background. 48

Figure 4-10 Represents a series of XPS spectra of Ru 3d peak collected from samples annealing in two different environments, Ar/H_2 and air, alternatively. Samples A and C are after annealed in Ar/H_2 (3%) atmosphere where samples B and D after annealed in air at 300C. 52

Figure 5-1 XRR data from a 4.6nm thick SiO_2 on a 20.8nm-thick Ru (0001) layer. (a) upper (black) curve is for measured data shifted by a factor of 10 for clarity and (b) the lower (red) curve is the model prediction. 55

Figure 5-2 XPS data for Ru 3d (a), Si 2p (b), and O 1s (c) for the same sample following the 2nd (blue) 4th (green), and 5th (red) stage in the annealing process described in Table 3-2. Ru^0 and $Ru^{\delta+}$ in figure 5-2(a) correspond to metallic ruthenium and ruthenium oxide (RuO_2) respectively. 56

Figure 5-3 LEED images at 68 eV for an air exposed (a) Ru/SiO_2 and (b) Ru/Al_2O_3................. 58

Figure 5-4 Resistivity and calculated upper surface specularity for the FS model as a function of evaporated SiO_2 thickness for 20 nm thick Ru samples. 60

Figure 5-5 Film resistivity and FS model upper surface specularity (p_u) as a function of sample processing. Shown are average values for the five samples with error bars to reflect the extreme values amongst the five.. 61

Figure 5-6 Shows (a) Ru metal thickness change, (b) RuO_x, (c) Ru oxide to Ru metal ratio, (d) Ru roughness and (e) surface specularity (p) processing as a function of sample shown are average values for the five samples with error bars to reflect the extreme values amongst the five. 63

Figure 5-7 The comparison between the XRR of RuO_x layer and the XPS Ru^+/Ru^0 ratio........... 64

Figure 5-8 Film resistivity, RuO_x, Ru metal thickness, and roughness as a function of sample processing. Shown are average values for the three samples with error bars to reflect the extreme values amongst the three. 66

Figure 6-1 XRD for a Ru film on sapphire $(11\bar{2}0)$ deposited at 500ºC with thickness d = 39.7 nm 69

Figure 6-2 The ϕ scan of Ru thin film on sapphire $(11\bar{2}0)$ 70

Figure 6-3 The ϕ scan of sapphire $(11\bar{2}0)$ 71

Figure 6-4 The resistivity of Ru 40 nm on sapphire $(11\bar{2}0)$ 72

Figure 6-5 The 2θ scan of Ru thin film on sapphire $(10\bar{1}0)$. 73

Figure 6-6 The resistivity of Ru 40 nm on sapphire $(10\bar{1}0)$ 74

Figure 6-7 The 2θ scan of Ru thin film on sapphire $(10\bar{1}2)$ 75

Figure 6-8 The resistivity of Ru 40 nm on sapphire $(10\bar{1}2)$ 76

Figure 6-9 The 2θ scan of Ru thin film on sapphire $(10\bar{1}4)$ 77

Figure 6-10 The resistivity of Ru 40 nm on sapphire $(10\bar{1}4)$ 78

LIST OF TABLES

Table 1-1 Oxygen affinity of metals expressed as the required O_2 vapor pressure (P_{O2}) for the oxide to be in thermodynamic equilibrium with the metal at 1000K. 3

Table 3-1 Listing of sample series studied. 31

Table 3-2 Thickness, roughness, and resistivity of Ru 10-80 nm that deposited at different temperature and annealed at 700°C in one atmosphere of flowing Ar/H_2 3% 33

Table 3-3 Process sequence with the primary characterization results for the third sample series consisting of 20 nm Ru films deposited at 700°C. 35

Table 3-4 Process sequence with the primary characterization results for the fifth sample series consisting of 20 nm Ru films deposited at 700°C. Data from the five samples are shown in a consistent sequential order in each cell of the table, except for the $Ru^{\delta+}/Ru^0$ ratios determined from XPS where only the same two of the five samples were characterized. 37

Table 3-5 Process sequence with the primary characterization results for the sixth sample series consisting of 20 nm Ru films deposited at 700°C. Data from the three samples are shown in a consistent sequential order in each cell of the table. 38

Table 4-1 Listing of FS model parameters 50

Table 6-1 The thickness, roughness, and resistivity of Ru 40 nm thin films on sapphire $(11\bar{2}0)$. 71

Table 6-2 The thickness, roughness, and resistivity of Ru 40 nm thin films on sapphire $(10\bar{1}0)$. 74

Table 6-3 The thickness, roughness, and resistivity of the Ru 40 nm thin films on sapphire $(10\bar{1}2)$. 76

Table 6-4 The thickness, roughness, and resistivity of Ru 40 nm thin films on sapphire $(10\bar{1}4)$. 77

CHAPTER 1 INTRODUCTION

1.1 Ruthenium

Ruthenium is a transition metal and it is element number 44 with atomic weight 101.07. It occupies the middle of the d-block in the periodic table. The valence electron configuration for ruthenium is ($4d^7$, $5s^1$) which spreads the valance electrons across more than one shell. Ruthenium has ten oxidation states ranging from -2 to + 8 that allow it to form many compounds. Ruthenium is from the platinum group along with Os, Rh, Ir, Pd, and Pt. Below its melting temperature of 2,334°C, Ru has a hexagonal close packed (hcp) crystal structure formed by the ABA sequence of stacking atomically close-packed planes [1]. Figure 1.1 shows the crystal structure and ABA stacking sequence of Ru, where the atoms are modeled as hard spheres.

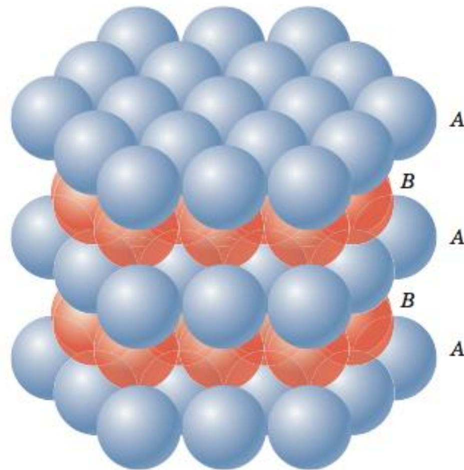

Figure 1-1 The hcp crystal structure with ABA stacking.

The crystalline character of Ru provides for anisotropy, and hence the identification of primary crystalline directions and planes is important. These are commonly designated using the Miller-Bravais indices where the symbol (hjkl) is used to identify planes and [hjkl] to identify

directions, where h,j, k, and l are integers. Figure 1.2 (a) identifies the basal plane as the (0001) plane and is the plane containing the darkened circles. Figure 1.2 (a) also identifies the [0001] direction by the arrow that is perpendicular to the (0001) plane. Figure 1.2 (b) similarly identifies the $(11\bar{2}0)$ plane and $[11\bar{2}0]$ direction while Figure 1.2 (c) identifies an $(10\bar{1}0)$ plane and $[10\bar{1}0]$ direction. From the symmetry of the structure it is evident that there are equivalent planes and equivalent directions, and these are notationally indicated by {hjkl} for a family of planes equivalent to (hjkl) and <hjkl> for a family of directions equivalent to [hjkl] [2].

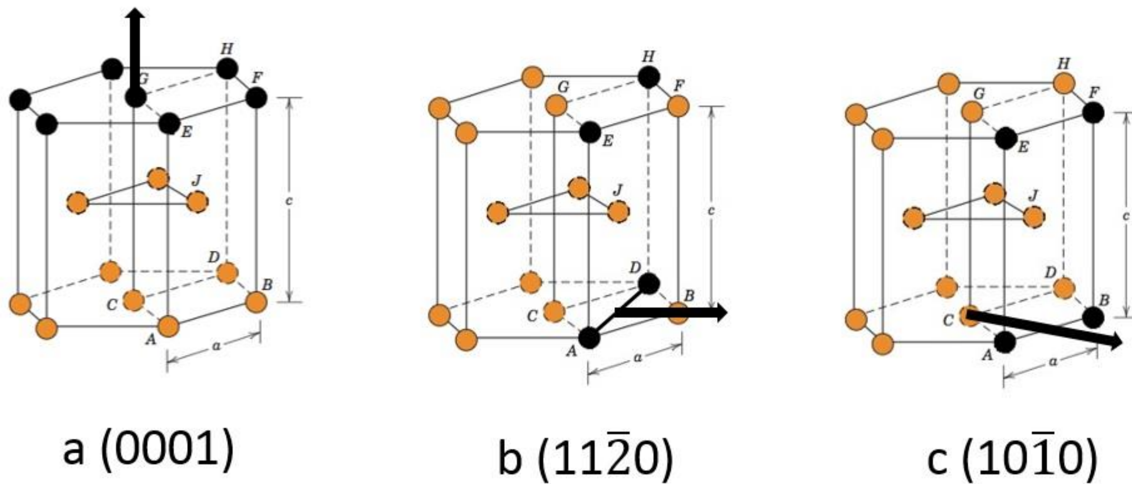

Figure 1-2 The hcp crystal structure, (a) identifies the basal plane as the (0001) plane and is the plane containing the darkened circles. Figure 1.2 (a) also identifies the [0001] direction by the arrow that is perpendicular to the (0001) plane. Figure 1.2 (b) similarly identifies the $(11\bar{2}0)$ plane and $[11\bar{2}0]$ direction while Figure 1.2 (c) identifies an $(10\bar{1}0)$ plane and $[10\bar{1}0]$ direction.

1.2 Ruthenium oxidation

Ru is inert to most chemicals over a broad range of temperatures. It is a near-noble metal, having an oxygen affinity greater than Au, Ag, Pt and Pd, but less than that of Cu, Pb, Ni, and Si. For example, Ru metal will not readily oxidize in air at room temperature, but easily forms RuO_2 above 800°K [3-4].

Table 1-1 Oxygen affinity of metals expressed as the required O_2 vapor pressure (P_{O2}) for the oxide to be in thermodynamic equilibrium with the metal at 1000K.

Metal, Oxide	P_{O2}, (atm)
Au, Au_2O_3	$10^{5.5}$
Pd, PdO	$10^{1.1}$
Ir, IrO_2	$10^{-0.9}$
Ru, RuO_2	$10^{-0.98}$
Rh, Rh_2O	$10^{-4.2}$
Cu, Cu_2O	$10^{-9.6}$
Ni, NiO	$10^{-16.2}$
Cr, Cr_2O_3	$10^{-30.1}$
Si, SiO_2	$10^{-36.3}$
Al, Al_2O_3	$10^{-47.2}$
Ca, CaO	$10^{-55.5}$

Ru has many naturally occurring isotopes with masses 9, 98, 99, 100, 101, 102, and 104. The properties of Ru more closely resemble those of Os (also having a hcp crystal structure) than those of Fe. Ru is a hard grayish-white metal and is used in metal alloys to increase hardness, primarily with platinum and palladium alloys. It has application as a water-resistant material in the electronics industry and as a catalyst in industrial fields. It is a p-type conductor. It is a relatively rare element comprising around 10^{-7}% of the earth crust [5].

The major application of Ru is as thin film resistors and buffer layers in the electronic industry. Ru is known as an essential homogeneous catalyst to reduce nitric oxides with hydrogen and is a very active catalyst to produce ammonia. Ru is a good oxidation catalyst in the mbar range, but under ultra-high vacuum UHV conditions the Ru (0001) is weak catalyst to oxidize CO to CO_2 [6]. Surface science studies, under UHV conditions, have shown a variety of structures of oxygen on the Ru (0001) surfaces exposed to oxygen. These are shown in the figure below and known as superstructures when the oxygen atoms take up positions consistent with the Ru surface atoms but with a scale expanded by an integer value. For example, a (2x2) superstructure would have an oxygen atom associated with every other Ru atom position along two different (not colinear) directions in the surface plane. The (2x2) oxygen superstructure is known to form on the Ru (0001) surface with an oxygen coverage of 0.25 monolayer at 400K [7]. At a coverage of 0.5 monolayer and 450K the (2x1) structure is known to form [8].

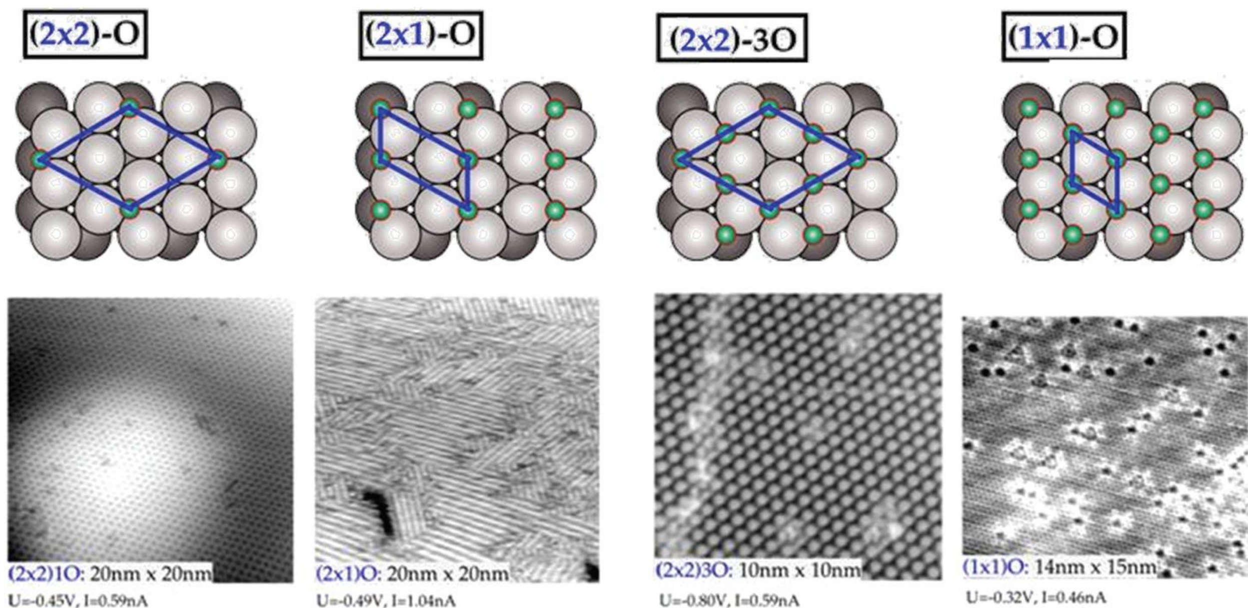

Figure 1-3 STM images show the chemisorbed oxygen on Ru (0001).

At greater oxygen coverage and higher temperature (about 500 K), the Ru (0001) surface is able to form two additional superstructures, the (2x2)-3O at 0.75 monolayer [9] and (1x1) structure at 1.0 monolayer [10]. The infrared spectroscopy of the O-Ru stretch vibration is increased when the O monolayer increased from 521 cm^{-1} (2x2) O of 0.25 monolayer to 585 cm^{-1} for (2x1)O of 0.5 monolayer, and the peak at 521 cm^{-1} decreases in intensity due to more O_2 exposure on Ru (0001) surface and the peak shifts up to 585 cm^{-1}. With increased temperature up to 600K with high O_2 exposure on the Ru (0001) surface, the peak at 585cm^{-1} disappears and a peak at 640 cm^{-1} shows up due to the increase of the oxide layer to 0.75 monolayer to (2x2) 3O. At a higher temperature around 800K, 1.0 monolayer of RuO_2 (110) forms on Ru (0001) and the stretch vibration of (1x1) O is 646 cm^{-1} [11-15].

The chemisorbed O on RuO_2 is weaker than O on Ru (0001), evidenced by the desorption temperature of chemisorbed O is higher than decomposition temperature of RuO_2 in UHV

conditions [16]. The different superstructures can be considered different thermodynamic phases and Figure 1.4 is a plot of the free energy of formation of the phases as a function of oxygen chemical potential (indicated as a partial pressure at 300K and 600K) to compare their relative stabilities [17].

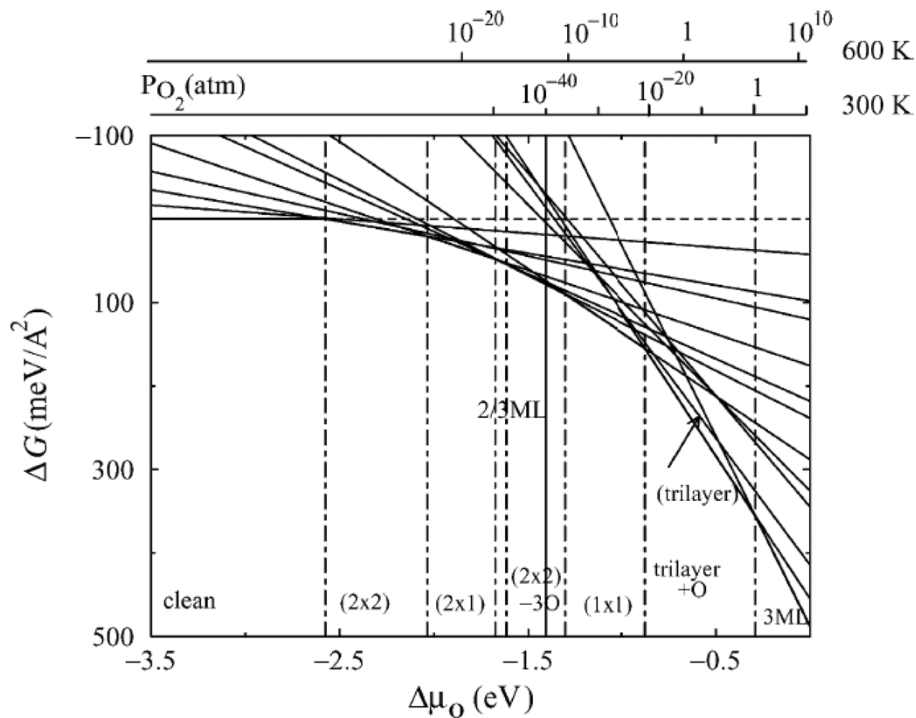

Figure 1-4 Calculated free energy O-Ru (0001) structures.

At temperatures of about 500K or below, the exposure of the Ru (0001) surface to oxygen does not result in the formation of a RuO_2 layer on the surface, but at temperatures in range 600-800 K the oxygen atoms start to form several monolayers of RuO_2 on Ru (0001) surface [18]. RuO_2 thin films with a (110) orientation have been observed to preferentially grow as a very flat layer on the Ru (0001) surface at temperatures above 550K. This is surprising, as the (110) RuO_2 surface is incommensurate with the Ru (0001) surface. The RuO_2 (100) surface is nearly epitaxial

on the Ru (0001) forming a (2x2) epitaxial superstructure and a rough RuO_2 (100) film has been grown on the Ru (0001) surface by electro chemical oxidation [19,20]. These epitaxial relations are shown in Figure 1.5.

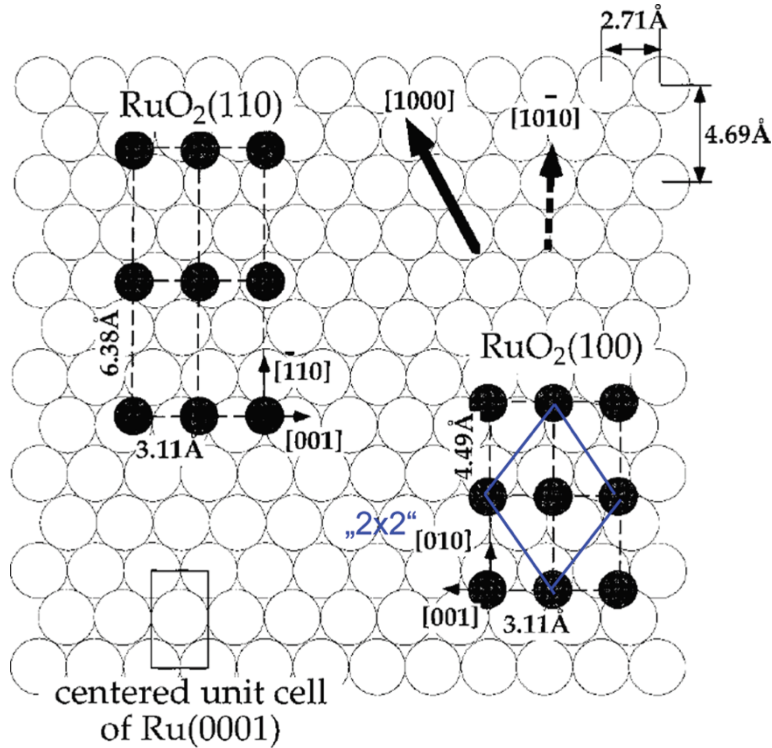

Figure 1-5 The RuO_2 (110) and RuO_2 (100) on Ru (0001) substrate.

Forming a RuO_2 layer on Ru (0001) from oxygen adsorption is structurally complex because the different oxygen superstructures on the Ru (0001) surface and the RuO_2 layer that formed is rough [21]. While a monolayer of RuO_2 (110) can grow on Ru (0001) surface at 600-800K in a rectangular stripe morphology [22], most experiments on Ru (0001) showed the RuO_2 films forming from isolated clusters [23].

1.3 Reduction of RuO_2 (110) on Ru (0001) surface

The RuO_2 which formed on a Ru (0001) surface that raises the Ru resistivity can be easily reduced. There are many methods to reduce RuO_2 (110) to Ru metal by exposing the RuO_2 with reducing agents, such as H_2, CO, or methanol at temperature above 150°C. Another way is by heating in vacuum to 550-700°C.

1.3.1 Reduction by hydrogen

Consistent with its relatively low affinity for oxygen, RuO_2 can be reduced to Ru metal fairly easily and reduction by H_2, CO and Methanol has been reported. The reduction of the RuO_2 (110) surface by hydrogen exposure at 413K was studied with in situ surface x-ray diffraction [6]. At a temperature around 390K the hydrogen molecules can reduce the RuO_2 (110) surface slightly, while it is hard to reduce the RuO_2 (110) by hydrogen at room temperature because the layer of water that forms on RuO_2 surface is strongly physiosorbed and cannot leave the surface. Figure 1.6 shows the reduction of RuO_2 on Ru (0001) via H_2 at various temperatures.

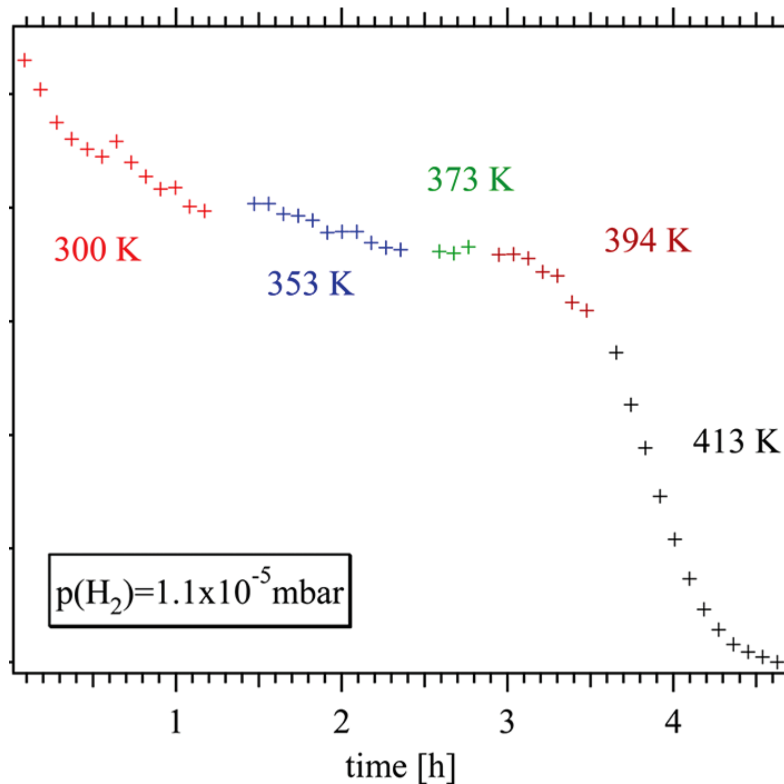

Figure 1-6 Surface X-ray diffraction explain the reduction of RuO_2 on Ru (0001) surface via H_2 molecules at various temperatures.

1.3.2 Reduction by carbon monoxide

At low pressure, around 10^{-5} mbar, and a temperature of 420K and an exposure of one-hour, CO molecules can reduce a monolayer of RuO_2 (110) on a Ru (0001) surface. Blume et al. studied the reduction of RuO_2 on a Ru (0001) surface via high pressure XPS and they found the temperature an important factor wherein below 400K the CO molecules could not fully reduce the RuO_2 [24,25].

1.3.3 Reduction by methanol

In a pressure of 10^{-6} mbar and temperature above 520K, methanol is a good reduction agent to reduce the RuO_2 (110) on Ru (0001). These results done by in situ at pressure 10^{-6} in XPS [26].

CHAPTER 2 BACKGROUND AND MOTIVATION

2.1 Resistivity of thin metal films

The observation of the increase in resistivity for thinner metallic conductors dates back to 1901 [27] and is commonly described as the resistivity size effect. The resistivity size effect was described by the semi-classical Fuchs-Sondheimer (FS) model in the middle of the last century [28,29]. This model attributes the resistivity increase to additional electron scattering from conductor interfaces (surfaces and grain boundaries) when the spacing between such events approaches the electron mean free path (λ) associated with phonon scattering. The FS model includes both the surface characteristics and film thickness as parameters. The resistivity of thin metal films has been primarily studied from two perspectives:

1. The surface science community has studied the change in resistivity of a fixed thickness of a metal film with an atomically clean surface as the gas species have been absorbed and desorbed from the surface, with the resistivity generally increasing with the coverage of the surface by the absorbent species. These studies focus on the surface characteristics relationship to resistivity, but rarely include thickness effects, due to the experimental difficulty in control of film thickness during the surface preparation.
2. The thin film community has studied the change in resistivity as a function of thickness for films having the same surface conditions, typically laboratory air exposed and contaminated.

Recently, interest in the resistivity size effect has been renewed as the dimension of the wires interconnecting transistors in integrated circuits approach the electron mean free path (EMFP), commonly designated by λ (which for Cu at room temperature is 39 nm) [30] and has become a "Critical Challenge" in the International Technology Roadmap for Semiconductors [31]. The wires in integrated circuits are typically not atomically clean and readily available for experiments based on the controlled absorption of gas molecules. Rather, they are buried within layer of a low-density amorphous silicon oxide dielectric, which makes the study of surface scattering at the metal surface of the wires more difficult. This dissertation addresses this challenge by a study of surface scattering at such a buried metal/dielectric interface and demonstrates a means to increase specular scattering at the interface, allowing a lower resistivity to be obtained.

2.2 Adsorbate induced changes in resistivity of atomically clean metal films

It has been widely observed that for an atomically clean conductor surface, an increase of resistivity can be observed due to atomic or molecular gas absorption on the surface. This is illustrated in Figure 2-1 where the resistivity increases with the number of surface absorbed species, n, and is seen to plateau at higher coverages. It should also be noted that this effect is more pronounced for thinner conductor layers where a greater fraction of the conduction electrons is near the surface.

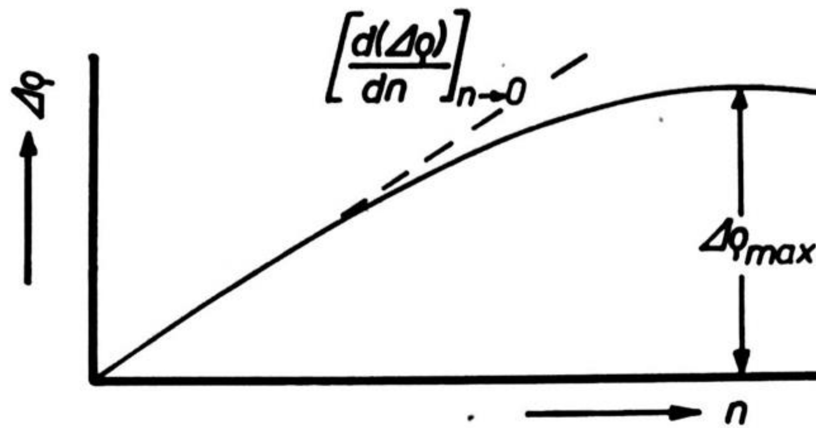

Figure 2-1 Resistivity increased due to gas adsorption on a thin film conductor.

There are four theories within the surface science community that have been proposed to understand the resistivity change due to molecules or atoms absorbing on the surface of a thin film [32].

2.2.1 Suhrmann model

Suhrmann [33] attempted to treat the increase in resistivity due to adsorption of a gas on the thin film, figure 2-2a by assuming that the adsorbed atoms or molecules coupled strongly to the conduction electrons on the surface and thereby decreased the number of free electrons within the thin film

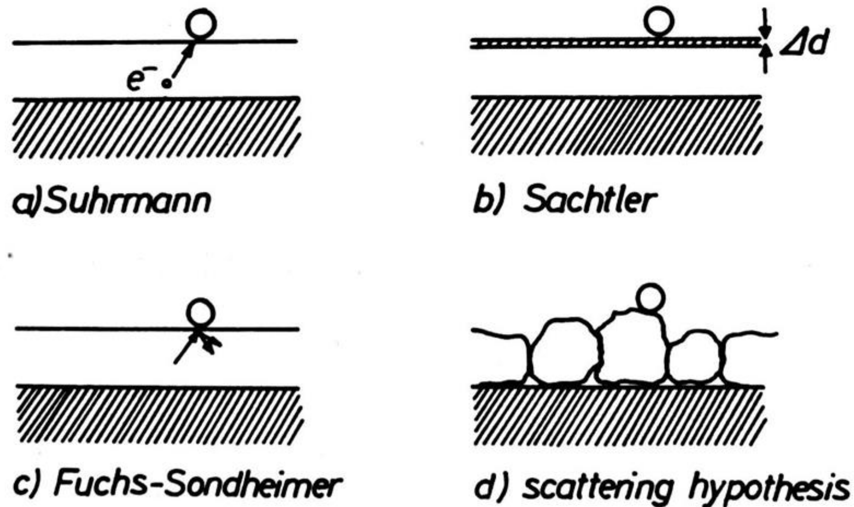

Figure 2-2 Four theories that have been proposed to understand the resistivity change due to molecules or atoms absorbing on the surface of a thin film.

The thickness, *h,* of the thin film and the EMFP, λ, remain unchanged and due to the chemical binding of the electrons the upper layer of the metal surface will lose its metallic properties according this equation.

$$\lim_{n\to 0} \frac{\mathrm{d}\,(\Delta\rho/\rho)}{\mathrm{d}n} = \mathrm{K}_1/h \qquad (2\text{-}1)$$

Where ρ is resistivity, *h* thickness, and K_1 is an initial proportionality constant describing the slope of the resistivity increase with absorbent coverage.

This model failed to account for the extent of the resistivity increase with coverage and also did not correctly describe the tendency of some adsorbed molecules to donate electrons to the surface and has since been widely discounted [32].

2.2.2 Sachtler model

In this model the resistivity increase with molecular absorption depends on film thickness and annealing temperature according to:

$$\lim_{n\to 0}\frac{\mathrm{d}\,(\Delta\rho/\rho)}{\mathrm{d}n} = K_2(h, T_A)/h \qquad (2\text{-}2)$$

Where K_2 is the initial proportionality constant, now dependent on both h and the annealing temperature, T_A. The model describes the resistivity increase as due to a loss of conductor thickness as a product layer is formed on the surface. This type of resistance increase is observed. For example, as a Ni film is oxidized, its resistivity can be described with this model. But the model fails to describe the increases in resistivity observed at a constant conductor layer thickness that are more scientifically interesting [32].

2.2.3 Fuchs-Sondheimer model

The Fuchs-Sondheimer (FS) model is most widely accepted model to describe the resistivity size effect and treats both film thickness and surface characteristics. It will be used extensively in this dissertation. It is a semiclassical model and treats the interaction of the conduction electrons with the surface as having two possible outcomes. In one case the electron incident upon the surface reflects back into the interior of the conductor with no loss of momentum. This is considered a "specular" reflection from the surface and these events do not contribute to resistivity, as the electron maintains its velocity obtained from the electric field prior to the collision with the surface, which is necessarily in a direction parallel to the surface. The other case is considered a "diffuse" reflection, and this is when the electron is modeled to leave the surface with a loss of momentum, specifically to return to the conductor interior in a random direction

with a velocity consistent with the local thermal equilibrium. The primary parameter of the model is the surface specularity, p, which is equal to one for fully specular surfaces and equal to zero for fully diffuse surfaces [28,29]. In this model the gas adsorption on the surface will decrease p and increase resistivity according to

$$\lim_{n\to 0} \frac{\mathrm{d}\,(\Delta\rho/\rho)}{\mathrm{d}n} = \mathrm{K}_3(\rho_o\lambda_o)/h \tag{2-3}$$

where ρ_o is the resistivity of an infinitely thick film (i.e., bulk resistivity) and λ is the EMFP for scattering in thick films.

2.2.4 The scattering hypothesis

The scattering hypothesis attributes the increase in resistivity to a variety of mechanisms that can contribute to the surface scattering. The surface roughness (as a fraction of film thickness) may increase, especially for metals on an insulating substrate, the impurity contamination level may also increase for thinner films (e.g., due to diffusion from the substrate, poor vacuum practices), and thinner polycrystalline films tend to have a smaller grain size which provides for an increase in grain boundary scattering. All of these can increase the resistivity response to absorbed gas species. The role of grain boundary scattering has been treated by semiclassical models similar to that of FS [34] and can be combined with the FS model for polycrystalline films [35]. This dissertation will focus on the resistivity of single crystal films, and hence the grain boundary scattering models do not apply. The film purity is clearly an important experimental variable and commonly controlled by use of inert substrates (single crystal sapphire in this work)

and high purity starting materials. The effect of roughness on resistivity is modelled separately and at very high roughness the porosity of a film can contribute to gas absorption phenomena.

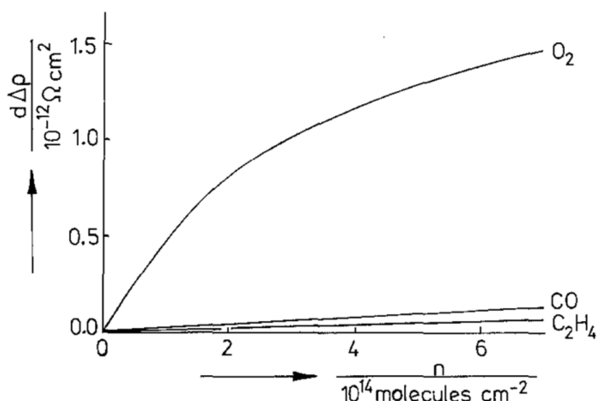

Figure 2-3 The resistivity effect of O_2, CO, and C_2H_4 adsorption on Ag thin films.

The surface adsorption of atomic and molecular gaseous species on the surface of transition metals has been studied extensively in the past. Silver thin films were covered step by step with O_2, CO, and ethylene at 77K, and the Ni surface readily interacts with gases in the atmosphere, especially with CO molecules which decompose on Ni. The atomic adsorbate species examined include H, N, O, S, and C [36-40], While the molecular species include N_2, CO, NO, NH_3, C_2H_4 and HCN [41-43]. The resistivity of the thin films initially increases linearly with the increase of the number of atoms or molecules on the thin film surface. This phenomenon was studied via FTIR, with a change in broadband in the IR reflectance surface metal and the coverage molecules due to the connection between the surface and the adsorption molecules. This lead to change the resistivity of metal. The local potential at the metal surface created due to the adsorbate is believed

to increase the scattering of conduction electrons by changing the electron density and increasing the surface roughness of the metal films [44-54].

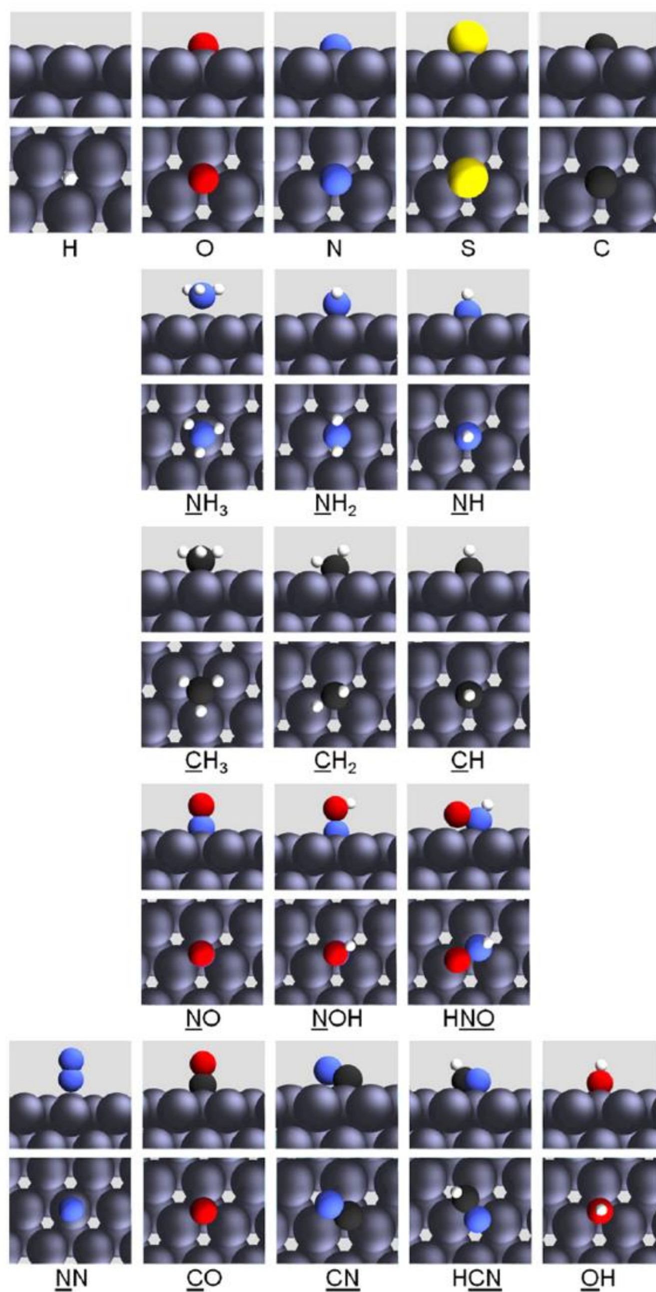

Figure 2-4 Various adsorbates on Ru (0001).

2.3 Resistivity due to variation of metal film thickness

The resistivity size effects due to grain boundaries [55-57], surface roughness [58-60], and scattering at the conductor surfaces [61-64] have been previously described and there is significant interest in obtaining "specular" metal surfaces with reduced surface scattering to minimize the size effect resistivity increase [62,65]. In this dissertation, a study of variations in scattering from the surface of single crystal Ru metal films with variation of the structure and chemistry of the surface is reported. Interfaces that are significantly specular, air-stable, and resilient to non-reversible changes, even when encapsulated beneath a dielectric, are observed and described. Within the surface science literature there are similar studies of resistivity effects due to surface scattering at metal/vacuum interfaces wherein the adsorption of atoms or molecules on the surface increases the electrical resistivity of the thin films. These chemical and structural modifications to the surface are known as adsorbate-induced changes where the electrical resistivity increases with increased coverage of the adsorbate species on the surface. This increased coverage is understood to increase the density of scattering sites on the surface. [32]. The adsorbate species can also form molecular compound complexes with the metallic thin films and thereby change the electronic states at the surface [66]. Thus, for a careful study of the resistivity size effect more than just the film sheet resistance and thickness are needed. In addition, the roughness, structure and chemistry of the surface must be known, and processing details, such as the annealing temperature, are also desired to provide insight to the surface characteristics. These prior studies typically explored variations in surface chemistry or structure at an exposed metal/vacuum or metal/vapor interface. Other prior work includes studies of large-scale roughness [58] and atomic scale roughness induced resistivity

wherein the presence of atomically flat regions on the metal surface were found to reduce surface scattering [67].

Ru, being a nearly noble metal from the platinum group, is being investigated by researchers for semiconductor applications. Ru has desirable properties that may allow it to replace Cu as an interconnect metal, such as high electrical conductivity, large work function, and small resistivity size effect. Nanoscale Ru may have lower resistivity than nanoscale Cu and can be expected to have greater stability due to its higher melting point [65, 68-72]. Ruthenium has also been studied as a diffusion barrier in the copper metallization process [5] and has potential for integration in semiconductor manufacturing, i.e., it known to be compatible with semiconductor manufacturing facilities and not pose a threat of contamination and yield loss. The electrical resistivity of RuO_2 is about 35.2 $\mu\Omega\cdot$cm at room temperature and higher than that of polycrystalline metallic ruthenium (about 7.36 $\mu\Omega\cdot$cm).

The encapsulation material used in our studies, SiO_2, has been used in many modern technologies and is studied here as an example of an amorphous dielectric. In contrast, recent studies of thin ordered silicon dioxide films grown on Ru (0001) have used XPS, low energy electron diffraction (LEED), and scanning tunneling microscopy wherein these techniques were used to study the epitaxial growth of SiO_2 layers on Ru (0001).

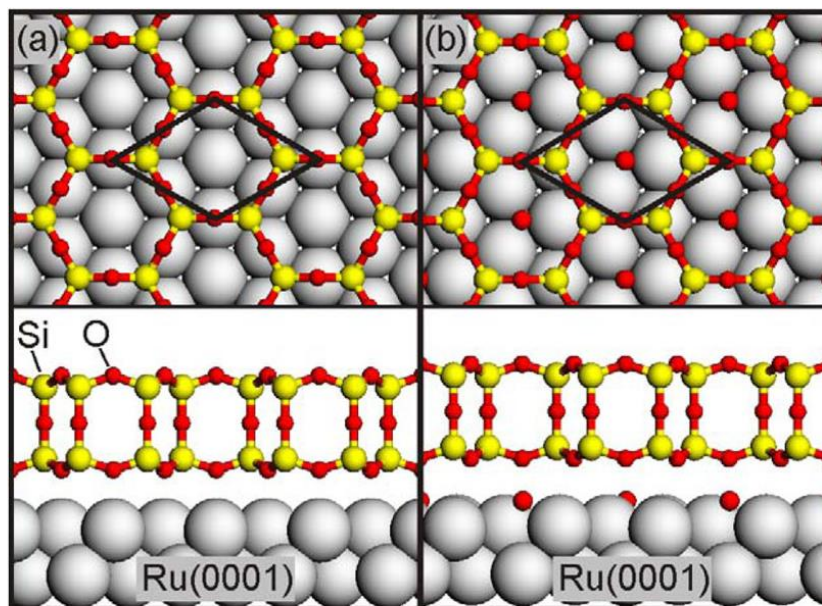

Figure 2-5 SiO_2 on Ru (0001), (a) O-poor (b) O-rich.

A silicon dioxide thin film when grown as a monolayer consists of SiO_4 tetrahedra that form a strong bond with Ru (0001) surface due to corner sharing of Si-O-Ru bonds. The limitation for this is the stoichiometry of the silicon dioxide, which is usually $SiO_{2.5}$ and not SiO_2 because not all SiO_4 tetrahedron corners are shared with another SiO_4 tetrahedron. When the silicon dioxide thickness is increased beyond a monolayer, the film forms a bilayer of two strongly bonded corner-sharing SiO_4 tetrahedron that have only weak bonding to the Ru (0001) surface, as the bonding to the Ru surface is due to dispersive forces and not by the monolayers of Si-O. The range of amorphous silicatene rings are from 4-membered to 9-membered rings, while the crystalline silicatene layer has only 6-membered rings [73-76].

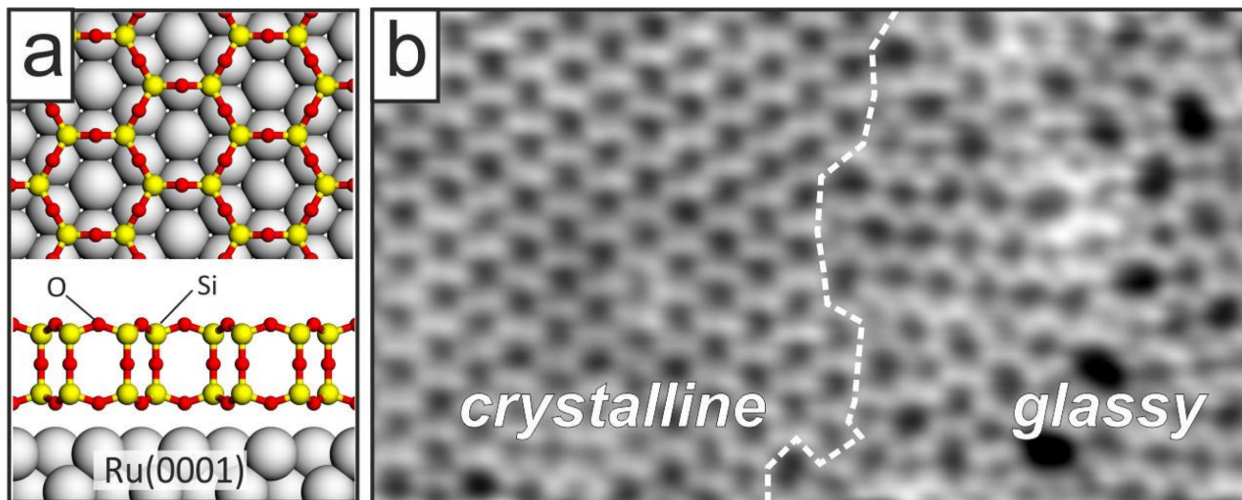

Figure 2-6 (a) Atomic structure of an ideal double-layer silicatene on Ru (0001). (b) STM image of crystalline and amorphous structures of the silicatene.

Another study of thin ordered ultrathin aluminum oxide film grown on Ru (0001) surface has used XPS, low energy ion scattering (LEIS), (LEED), scanning tunneling microscopy (STM) and high-resolution electron loss spectroscopy (HRELS) and deposited aluminum in an ambient of oxygen. The thin film growth at 300K is two-dimensional while the thin film growth at 1170K is three dimensional [77].

In the present work, we study amorphous SiO_2 and Al_2O_3 grown in vacuum at room temperature on epitaxial Ru (0001)/sapphire (0001) and focus on the interaction of the deposition itself and subsequent anneals in oxidizing and reducing gases on the buried SiO_2/Ru and Al_2O_3/Ru interfaces and relate these to changes in surface scattering. In the current work, resistivity measurements as a function thickness and as a function of chemical and/or structural changes at a buried metal/dielectric oxide interface are reported. X-ray photoelectron spectroscopy (XPS) is used to determine the chemical bonding at the buried interface, while X-ray reflectivity (XRR) is

used to determine interfacial roughness of metal upper surface. For the metal/dielectric interface study, we focus on single crystal 20 nm Ru on sapphire as our conductor and amorphous SiO_2. Our choice of the metal and dielectric is motivated by the different oxygen affinities of Si and Ru, which allows desirable control of experimental conditions at the metal/dielectric interface.

CHAPTER 3 EXPERIMENTAL

3.1 Introduction

The properties of thin films are reliant on many features such as substrate materials, substrate temperature, the technique of deposition, ambient gas pressure, and deposition rate. Modern technology can assist to deposit thin films with specific properties such as low porosity, thermal stability, adhesion, and desirable stoichiometry. There are many procedures for production of thin films such as physical vaper deposition (PVD), chemical vaper deposition (CVD), sol-gel, atomic layer deposition, and molecular beam epitaxy. Understanding of the growth procedures with careful control allows us to deposit thin films with specific thicknesses that can be on the atomic/molecular level and obtain suitable thin films. The quality of the thin film depends on the optimization of the deposition procedure. In this chapter the method by which the Ru, Ru/SiO_2, Ru/Al_2O_3 thin film samples are prepared, sputtering, is described in general. Subsequently, the characterization techniques for the samples, by X-ray diffraction (XRD), X-ray reflectivity (XRR), X-ray photoelectron spectroscopy (XPS), low energy electron diffraction (LEED), and four-point sheet resistance measurements are described, and the details of the specific processing used for the samples is described in detail.

3.2 Sputter deposition

Sputtering involves dislodging atoms or molecules from a target, the source material, to deposit on a substrate surface through the impact of gaseous ions. Evaporation and CVD techniques do not have advantages compared to sputtering, which can have easy control of

composition, and the thin films have more purity and can be deposited at lower temperature compared to CVD.

PVD techniques have a wide range of applications, from decorative films to high temperature superconductors. The rate of deposition can vary from angstroms to millimeters of film per minute. PVD techniques are suitable for many materials such as inorganic alloys and compounds as well as organic materials. The PVD coating of materials by deposition in vacuum often allows a unique ability to control material properties by controlling the bombardment of the growing film with ions, electrons, and neutral species during the deposition process. There are many PVD techniques that differ based on their ability to control the growth conditions. Cathodic arc deposition uses an arc discharge to generate ions of the film material which can then be directed towards the substrate with a wide range of controlled energies to effectively implant the ions into the film. This technique can provide very hard coatings (e.g., diamond-like amorphous carbon). Evaporation is a technique in which the film material is heated in vacuum to initiate sublimation or evaporation and the source atoms travel as non-colliding vapor atoms to the substrate where they condense back to a solid phase and form the film. Magnetron sputtering uses a controlled vacuum in which a partial pressure on an inert gas is maintained (typically Ar at ~5×10^{-7} atmospheres). A direct current (DC) a used for sputtering a conductive target while radio frequency (RF) is used for non-conductive targets.

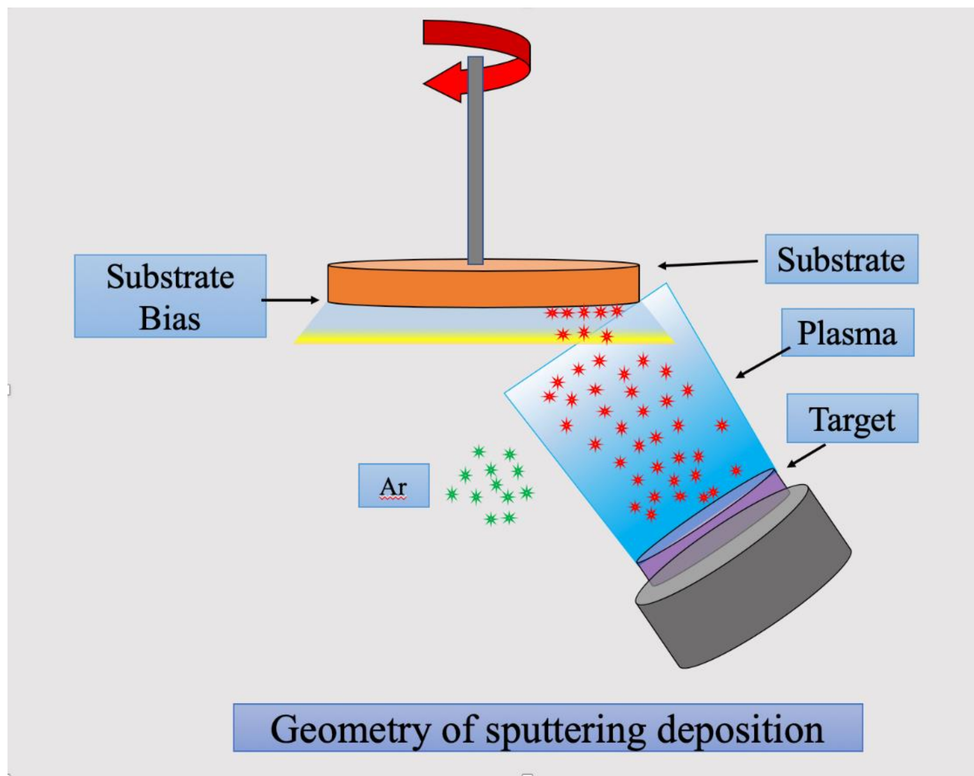

Figure 3-1 Geometry of sputtering deposition.

A negative voltage is present on a target composed of the material to be used to form the film. This voltage attracts positively charged inert gas ions that impact the target with sufficient energy to cause the release of target atoms (known as sputtering) as well as electrons. The former condenses on the substrate to form a film while the latter undergo collisions with the inert gas atoms, forming a plasma and maintaining a supply of ions to perpetuate the sputtering of atoms from the target. The presence of the plasma allows inert gas atoms or electrons to be attracted to the substrate for the bombardment to control film properties [77,78].

3.3 XRD and XRR characterization

3.3.1 XRD characterization

X-ray diffraction is a remarkable analytical technique to identify the crystalline structure of materials. This information is obtained from their diffraction pattern. That diffraction occurs when X-ray incident beam interacts with the atoms of the sample and is coherently scattered. The XRD studies reported here were performed using a Panalytical X'pert3 MRD system with a copper K_α radiation source (λ=1.54056A°) with a graded multilayer mirror for the incident beam and the 1D PIXcel detector for the diffracted beam.

3.3.2 XRR characterization

XRR is a technique that uses the full thickness of a thin film layer to form a coherent interference pattern. The layer thicknesses and roughnesses of our thin film samples were characterized by XRR with same X-ray optical configuration used for the XRD measurements. The XRR data were interpreted using the PANalytical X'Pert Reflectivity software. The samples without a SiO_2 or Al_2O_3 overlayer were modeled as a sapphire/Ru/RuO_2 structure, the samples with the SiO_2 overlayer as sapphire/Ru/RuO_2/SiO_2, and the samples with the Al_2O_3 overlayer as a sapphire/Ru/RuO_2/Al_2O_3 structure. Bulk density values of 3.989 g/cm^3, 12.4 g/cm^3, 6.97 g/cm^3, and 2.196 g/cm^3 were used for the sapphire, Ru, RuO_2, and SiO_2, respectively.

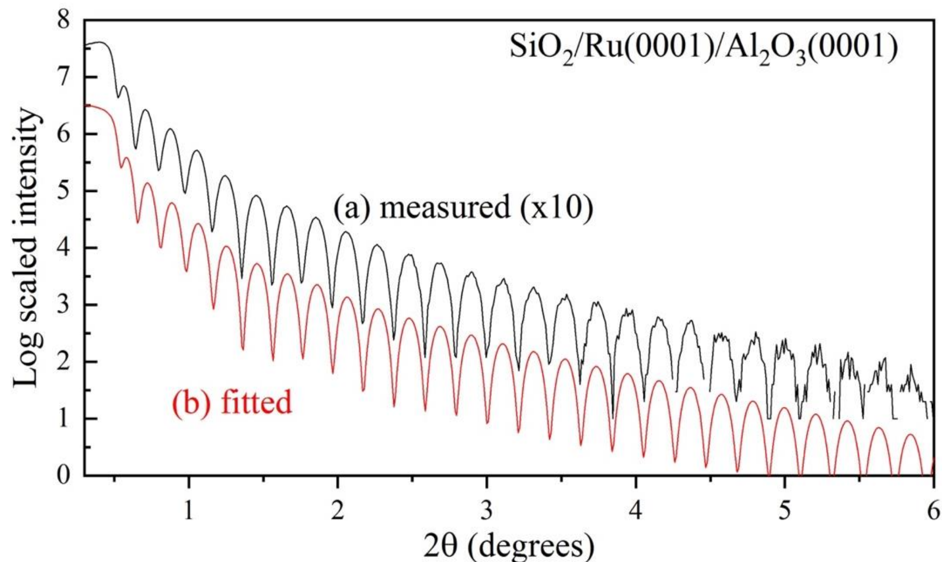

Figure 3-2 Representative XRR data from a 4.6nm thick SiO_2 on a 20.8nm-thick Ru (0001) layer. (a) upper (black) curve is for measured data shifted by a factor of 10^1 for clarity and (b) the lower (red) curve is for fitted model.

3.4 Four-Point Resistivity Measurement

The resistivity measurement is made in accordance to the delta (output voltage) measurement test circuit, see Fig 3-3, where in the Keithley source meter 2400 is a bipolar fixed-amplitude current source which reverses polarity at a fixed interval and communicates the polarity reversal to the Keithely nanovoltmeter model 2812 via the 8501 Trigger Link Cable. This allows resistance to be made independent of any thermally induced DC voltage that may be present. This resistance was measured in a sample contacted in the Van der Pauw geometry, which, as implemented, has less than 3% of error [79].

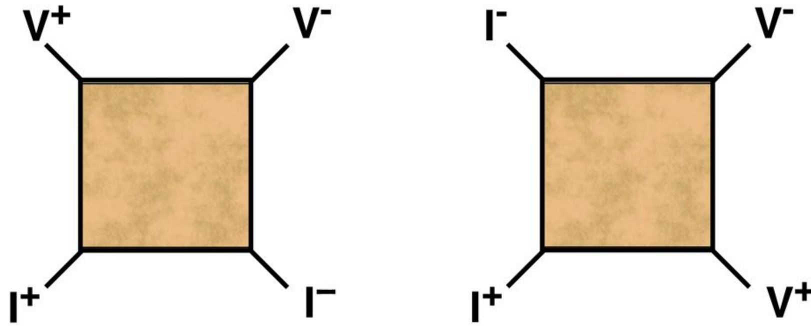

Figure 3-3 Diagram of the Van der Pauw geometry dipping probe

The resistance according to above figure is calculated as follows.

$$R_{1243} = \frac{V_{43}}{I_{12}} \quad (3\text{-}1)$$

where R= Resistance, V= Voltage, and I= Current

Where R_{1243} indicates where current was sourced 1→ 2 and voltage was measured 3 → 4. To calculate the sheet resistance, Rs, the van der Pauw method makes two measurements. First, it sources current along the horizontal edge of the film and measures the voltage drop across the opposite edge. Then it sources the current along the vertical edge of the film and measures the voltage drop across the opposite edge. The average vertical and horizontal resistances are calculated

$$R_{vertical} = \frac{R_{1243} + R_{4312}}{2} \quad (3\text{-}2)$$

$$R_{horizontal} = \frac{R_{1423} + R_{2314}}{2} \quad (3\text{-}3)$$

A numerical method is then used to solve for the sheet resistance, R_s

$$e^{(-\pi R_{vertical}/R_s)} + e^{(-\pi R_{horizontal}/R_s)} = 1 \quad (3\text{-}4)$$

expressed in ohms per square or Ω/□. Finally, the resistivity, ρ of the sample is determined as the product of R_s and the thickness, h [79-81].

$$\rho = R_s h \qquad (3\text{-}5)$$

3.5 Sample preparation details

The deposition and annealing of six series of Ru, Ru/SiO_2, and Ru/Al_2O_3 thin film samples are described in this chapter. The first, second, and third sample series are variations in thicknesses for Ru films on sapphire while the fourth, fifth, and sixth series utilize bilayered Ru/SiO_2 and Ru/Al_2O_3 at a single Ru thickness to elucidate surface scattering phenomena.

3.5.1 Ru single crystal film deposition

The Ru thin films were sputter deposited on single-side polished two-inch diameter (0001) Al_2O_3 sapphire substrates obtained from MTI Corporation. Prior to deposition, the as-received sapphire substrates were pre-conditioned by heating in a tube furnace in air at 1000°C for 30 minutes to remove adsorbed contaminants and loaded within the deposition chamber within 5 minutes to minimize the possibility of recontamination. The deposition system used was an ATC2200 UHV sputtering system obtained from AJA International Inc. equipped with a loadlock chamber for sample introduction and operated with a base vacuum in the low 10^{-8} Torr range. DC magnetron sputtering in a point-of-use purified Ar gas ambient at 4 mTorr from a two-inch diameter Ru (99.95%) target was used for the Ru film depositions. The Ru deposition power of 200W was used to obtain a deposition rate 0.13 nm/s. In the deposition chamber, the sapphire substrates were heated to 400°C, 500°C, 600°C, and 700°C (for sample series one) 350°C (for sample series two) or 700°C (for sample series three, four, five, and six) for 20 minutes prior to deposition and maintained at that temperature during the deposition process. The deposition time

was varied to obtain Ru films of the desired thickness. Six series of samples were prepared, as described in Table 1.

Table 3-1 Listing of sample series studied.

Sample Series	Ru Layer Thickness (nm)	Dielectric Overlayer	Deposition temperature
1	10 to 80	None	400°C, 500°C, 600°C, 700°C
2	8 to 124	None	350°C
3	20 to 80	None	700°C
4	20	SiO_2 Evaporation	700°C
5	20	SiO_2 Sputtering	700°C
6	20	Al_2O_3 Sputtering	700°C

Sample series one was made in the thickness range of 10 nm to 80 nm at temperatures ranging from 400°C to 700°C. Sample series two was made in the thickness range of 8 nm to 124 nm. Sample series three was made in the thickness range of 20 nm to 80 nm. The fourth, fifth, and six experimental series each consisted of samples cut from a single wafer, all having a deposited Ru thickness of 20 nm. After the initial Ru sputter deposition, the ruthenium thin films were allowed to cool to room temperature in the sputter deposition chamber and removed from the vacuum system and exposed to the ambient laboratory atmosphere. The sapphire wafers with deposited ruthenium thin films were subsequently cut into 7 mm by 7 mm square pieces by a CO_2 laser incident upon the back side of the wafer to avoid the laser reflection from the shiny Ru thin film, we found the optimal performance to cut the Ru thin films on sapphire was using speed 6 millimeters per second and power of 5W.

3.5.2 Anneal to 700°C

After cutting, samples series one was annealed at 700°C in one atmosphere of flowing Ar/H_2 3% wherein the annealing temperature was increased from room temperature to 700°C in 30 minutes and held for 120 minutes and allowed to cool to room temperature. The thickness and resistivity for these annealed sample are described in Table 3-2.

Table 3-2 Thickness, roughness, and resistivity of Ru 10-80 nm that deposited at different temperature and annealed at 700°C in one atmosphere of flowing Ar/H_2 3%

Deposit Temperature °C	Ru Thickness (nm)	Ru Resistivity before annealed (μΩ-cm)	Ru Resistivity after annealed (μΩ-cm)	Ru Roughness before annealed (nm)	Ru Roughness after annealed (nm)	RuO_x before annealed (nm)	RuO_x after annealed (nm)
400°C	72.83	13.9	10.19	1.35	0.17	0.54	0.26
400°C	38.13	15.2	10.4	1.22	0.14	0.47	0.27
400°C	19.58	15.52	11.45	0.90	0.16	0.40	0.23
400°C	9.88	19.32	12.48	0.65	0.17	0.43	0.23
500°C	82.48	11.69	10.61	1.37	0.22	0.61	0.25
500°C	38.72	12.09	10.80	1.12	0.15	0.52	0.25
500°C	19.67	12.53	11.28	0.53	0.14	0.39	0.20
500°C	9.78	15.62	11.68	0.53	0.15	0.41	0.22
600°C	78.31	9.85	9.65	0.67	0.18	0.49	0.28
600°C	39.70	10.32	9.92	0.68	0.18	0.43	0.23
600°C	19.78	10.8	10.40	0.40	0.15	0.37	0.24
600°C	10.1	12.48	11.12	0.37	0.14	0.38	0.22
700°C	80.8	9.56	9.39	0.20	0.14	0.37	0.25
700°C	39.21	9.56	9.41	0.29	0.15	0.37	0.23
700°C	19.78	10.03	9.98	0.25	0.13	0.34	0.23
700°C	10.06	11.05	10.79	0.26	0.16	0.32	0.20

3.5.3 Step anneal to 950°C

After cutting, all the samples were annealed (ex-situ) step-wise in one atmosphere of flowing Ar/H_2 3% to a maximum temperature of 950°C. The annealing temperature was increased from room temperature to 350°C and stabilized at 350°C for 30 minutes. After that the temperature was further increased in steps of 100°C and held for 30 minutes at each temperature. This increasing temperature portion of the anneal continued up to the maximum temperature of 950°C, at which temperature the sample was held for 30 minutes. Subsequently, the temperature was decreased in steps of 100°C and held at each temperature for 60 minutes until 150°C was reached, after which the sample was allowed to cool to room temperature. This was the basic processing (Ru film deposition and ex-situ 950°C Ar/H_2 step anneal) which was performed for all of the sample series 2 though 6.

3.5.4 Additional anneals for series 3

The third sample series was subjected to subsequent additional oxidizing and reducing annealing treatments of the Ru films. The anneals were in one atmosphere of Ar/H_2 3%, or air, at a temperature of 300°C wherein the desired temperature was held for 2 hours, and then furnace cooled to room temperature. These anneals and the sequence in which they were performed is described in Table 3-3.

Table 3-3 Process sequence with the primary characterization results for the third sample series consisting of 20 nm Ru films deposited at 700°C.

Process Step	Process	Resistivity (μΩ-cm)	Ru Thickness (nm)	Ru Oxide Thickness (nm)	Ru Roughness (nm)	XPS $Ru^{\delta+}/Ru^0$ Ratio
1	Deposit Ru	9.68	18.61	0.32	0.29	0.18
2	700°C Ar/H_2	9.49	18.58	0.26	0.15	0.08
3	950°C Ar/H_2	9.06	18.64	0.22	0.13	0.05
4	300°C Ar/H_2	9.08	18.59	0.22	0.13	0.06
5	300°C Air	9.53	18.12	0.64	0.17	0.21
6	300°C Ar/H_2	9.05	18.56	0.27	0.12	0.08
7	300°C Air	9.64	18.09	0.71	0.15	0.22
8	300°C Ar/H_2	9.15	18.53	0.26	0.13	0.07

3.5.5 SiO_2 overlayer depositions

For the fourth sample series, the Ru film coupons were overcoated with electron beam evaporated SiO_2 of thicknesses from 0.5 nm to 30 nm using an ATC2600 UHV evaporation system obtained from AJA International Inc. equipped with a loadlock chamber for sample introduction and operated with a base vacuum in the 10^{-8} Torr range. The deposition thickness and rate were monitored by a calibrated quartz crystal microbalance.

For the fifth sample series, the Ru film coupons were overcoated with a single 5 nm thickness of sputter deposited SiO_2 via radio frequency (RF) sputtering in 4 mTorr of argon at room

temperature with 165 W of power using a two-inch diameter SiO_2 (99.95%) target. The rate of deposition for SiO_2 on the ruthenium thin films was 0.03 nm/s. The thickness of the overlayer was chosen to be sufficiently thin to allow subsequent XPS characterization of the buried Ru/SiO_2 interface.

3.5.6 Al_2O_3 overlayer depositions

For sample series six, the Ru film coupons were overcoated with a single 6 nm thickness of sputter deposited Al_2O_3 via RF sputtering in 4 mTorr of argon at room temperature with 200 W of power using a two-inch diameter Al_2O_3 (99.95%) target. The rate of deposition for Al_2O_3 on the ruthenium thin films was 0.02 nm/s.

3.5.7 Additional anneals for series 5

The fifth sample series was also subjected to subsequent additional oxidizing and reducing annealing treatments of the Ru/SiO_2 bilayer films, including a repeat of the 950°C Ar/H_2 step anneal. The lower temperature anneals were in one atmosphere of one of the following gases: flowing Ar/H_2 3%, Ar/O_2 20%, or air, at temperatures 300°C, 400°C, or 500°C wherein the desired temperature was held for 2 hours, and then furnace cooled to room temperature. These anneals and the sequence in which they were performed is described in Table 3-4.

Table 3-4 Process sequence with the primary characterization results for the fifth sample series consisting of 20 nm Ru films deposited at 700°C. Data from the five samples are shown in a consistent sequential order in each cell of the table, except for the $Ru^{\delta+}/Ru^{0}$ ratios determined from XPS where only the same two of the five samples were characterized.

Process Step	Process	Resistivity (μΩ-cm)	Ru Thickness (nm)	Ru Roughness (nm)	Ru Oxide Thickness (nm)	SiO_2 Thickness (nm)	XPS $Ru^{\delta+}/Ru^{0}$ Ratio
1	Deposit Ru	9.41, 9.43, 9.38, 9.41, 9.46	20.74, 20.77, 20.73, 20.88, 20.55	0.25, 0.28, 0.26, 0.30, 0.23	0.29, 0.29, 0.30, 0.14, 0.36	-	0.17, 0.18
2	950°C Ar/H_2	9.00, 8.97, 8.96, 8.92, 8.93	20.85, 20.84, 20.88, 20.89, 20.59	0.12, 0.15, 0.13, 0.15, 0.11	0.10, 0.26, 0.24, 0.24, 0.26	-	0.07, 0.05
3	Deposit SiO_2	9.42, 9.40, 9.41, 9.42, 9.49	20.81, 20.81, 20.85, 20.91, 20.63	0.04, 0.04, 0.01, 0.03, 0.01	0.27, 0.25, 0.25, 0.26, 0.26	5.04, 4.83, 4.80, 5.02, 4.99	<0.01, <0.01
4	500°C Ar/H_2	8.93, 8.97, 8.95, 8.89, 8.92	20.82, 20.80, 20.80, 20.88, 20.61	0.14, 0.10, 0.08, 0.11, 0.09	0.25, 0.25, 0.23, 0.24, 0.26	4.78, 4.64, 4.74, 4.88, 4.79	<0.01, <0.01
5	500°C Air	9.38, 9.41, 9.38, 9.45, 9.63	20.22, 20.33, 20.39, 20.45, 20.23	0.25, 0.26, 0.19, 0.26, 0.32	1.46, 1.16, 1.17, 1.20, 1.97	4.80, 4.78, 5.01, 4.74, 4.82	0.75, 0.76
6	500°C Ar/H_2	9.10, 9.01, 8.95, 8.93, 9.00	20.81, 20.80, 20.81, 20.90, 20.63	0.11, 0.11, 0.09, 0.10, 0.09	0.28, 0.29, 0.27, 0.27, 0.27	4.67, 4.75, 4.60, 4.57, 4.57	0.03, 0.01
7	950°C Ar/H_2	9.09, 9.04, 8.98, 8,88, 8.95	20.84, 20.84, 20.95, 20.93, 20.68	0.05, 0.06, 0.05, 0.07, 0.12	0.26, 0.27, 0.27, 0.25, 0.27	4.57, 4.55, 4.77, 4.54, 4.58	0.05, 0.08
8	400°C Ar/O_2	9.53, 9.41, 9.24, 9.21, 9.22	20.79, 20.75, 20.67, 20.79, 20.47	0.19, 0.24, 0.21, 0.28, 0.22	0.53, 0.50, 0.48, 0.43, 0.52	5.38, 5.23, 4.91, 5.05, 4.94	0.70, 0.60
9	500°C Ar/H_2	9.33, 9.22, 9.08, 9.02, 9.04	20.80, 20.83, 20.83, 20.90, 20.61	0.10, 0.11, 0.13, 0.10, 0.15	0.25, 0.26, 0.23, 0.20, 0.28	4.79, 4.66, 4.73, 4.71, 4.67	0.03, 0.05
10	300°C Ar/O_2	9.43, 9.33, 9.11, 9.02, 9.07	20.72, 20.83, 20.79, 20.69, 20.56	0.15, 0.15, 0.13, 0.15, 0.10	0.23, 0.30, 0.24, 0.24, 0.24	5.31, 4.84, 5.44, 5.09, 5.15	0.38, 0.40
11	950°C Ar/H_2	9.16, 8.97, 8.92, 8.96, 8.95	20.88, 20.91, 20.94, 20,99, 20.72	0.17, 0.13, 0.09, 0.12, 0.17	0.20, 0.20, 0.25, 0.25, 0.12	5.20, 4.98, 4.81, 4.91, 4.98	0.06, 0.04

3.5.8 Additional anneals for series 6

The sixth sample series was also subjected to subsequent additional oxidizing and reducing annealing treatments of the Ru/ Al_2O_3 bilayer films, including a repeat of the 950°C Ar/H_2 anneal. The temperature anneals were in one atmosphere in Ar/H_2 3%, or air, at a temperature of 500°C wherein the desired temperature was held for 2 hours, and then furnace cooled to room temperature. These anneals and the sequence in which they were performed is described in Table 3-5.

Table 3-5 Process sequence with the primary characterization results for the sixth sample series consisting of 20 nm Ru films deposited at 700°C. Data from the three samples are shown in a consistent sequential order in each cell of the table.

Process step	Process	Resistivity (μΩ-cm)	Ru thickness (nm)	Ru roughness (nm)	RuOx thickness (nm)
1.	Deposit Ru	9.69, 9.70, 9.67	19.67, 19.80, 19.82	0.37, 0.34, 0.34	0.35, 0.29, 0.30
2.	950°C Ar/H_2	9.02, 9.03, 9.05	19.71, 19.83, 19.87	0.15, 0.14, 0.15	0.22, 0.19, 0.22
3.	Deposit Al_2O_3	10.09, 10,05, 10.13	19.66, 19.82, 19.84	0.15, 0.16, 0.14	0.18, 0.12, 0.19
4.	500°C Ar/H_2	9.32, 9.27, 9.36	19.69, 19.81, 19.79	0.13, 0.15, 0.15	0.21, 0.24, 0.25
5.	500°C Air	9.61, 9.58, 9.67	19.35, 19.39, 19.34	0.22, 0.24, 0.25	0.86, 0.97, 1.03
6.	500°C Ar/H_2	9.44, 9.42, 9.49	19.67, 19.70, 19.69	0.15, 0.15, 0.17	0.29, 0.32, 0.36
7.	500°C Air	9.88, 9.87, 9.94	19.31, 19.32, 19.28	0.24, 0.20, 0.21	0.91, 0.99, 1.06
8.	500°C Ar/H_2	9.68, 9.66, 9.72	19.62, 19.66, 19.59	0.12, 0.16, 0.17	0.38, 0.34, 0.39
9.	500°C Air	10.13, 10.09, 10.21	19.28, 19.30, 19.27	0.19, 0.21, 0.22	0.78, 0.95, 1.10
10.	500°C Ar/H_2	9.62, 9.72, 9.74	19.61, 19.68, 19.59	0.16, 0.16, 0.17	0.33, 0.35, 0.39
11.	950°C Ar/H2	9.52, 9.61, 9.66	19.69, 19.76, 19,77	0.16, 0.15, 0.17	0.23, 0.27, 0.30

CHAPTER 4 SINGLE CRYSTAL RUTHENIUM FILMS

The characterization of the Ru thin film samples by XRD, XRR, XPS, LEED, and four-point sheet resistance measurements are described in this chapter. The sheet resistance measurements were performed on each of the samples. The XRD and LEED characterization were performed on selected representative samples that shared the common basic processing.

4.1 X-ray diffraction

For selected samples, their single crystal nature was confirmed by XRD with specular theta-2theta scans and with non-specular phi-scans.

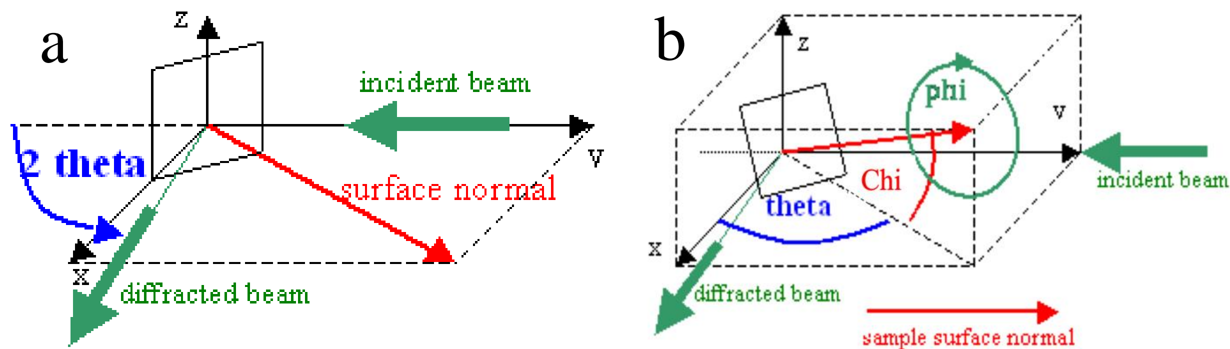

Figure 4-1 The diagram of (a) theta-2theta scan and (b) phi scan

An example of a specular scan exhibiting only the (0002) and (0004) peaks of Ru and the sapphire (0006) and (00012) peaks is shown in Figure 4-2 and establishes that one axis of crystal orientation is fixed out of the sample plane.

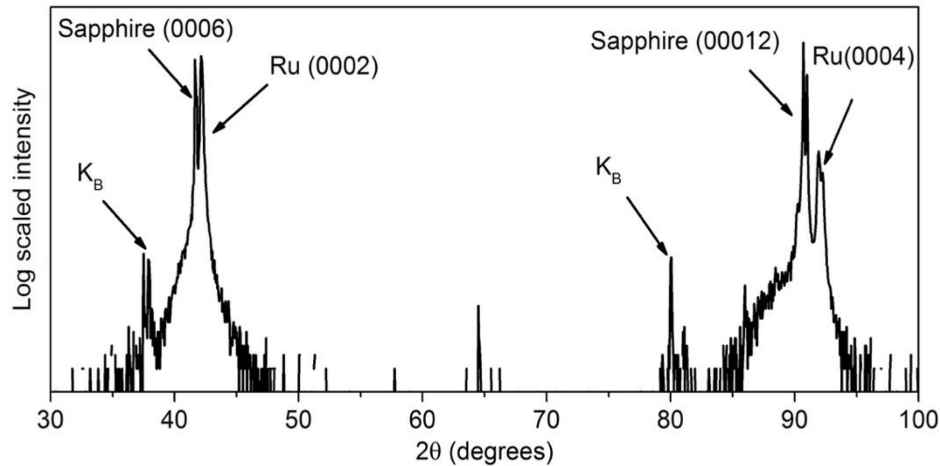

Figure 4-2 Specular XRD scan for a Ru film on sapphire (0001) deposited at 700ºC with thickness d = 39.8 nm.

Non-specular phi scans at chi equal to 57.71° and two-theta equal to 84.68° were performed to examine the crystallographic orientation of the Ru film crystallites within the sample plane. The six fold symmetry of the Ru $\{11\bar{2}2\}$ peaks was observed establishing that a single fixed in-plane crystallographic orientation is present. The combinations of the two fixed crystallographic directions for the crystallites establishes the film as single crystal in nature, i.e., all the crystallites present have the same orientation, hence they are not separate crystallites but part of a single large crystal. An additional non-specular phi scan at chi equal to 42.3° and two-theta equal to 57.499° was performed to observe the six-fold symmetry of the sapphire $\{11\bar{2}6\}$ peaks of the single crystal sapphire substrate. These two phi scans are shown in Figure 4-3.

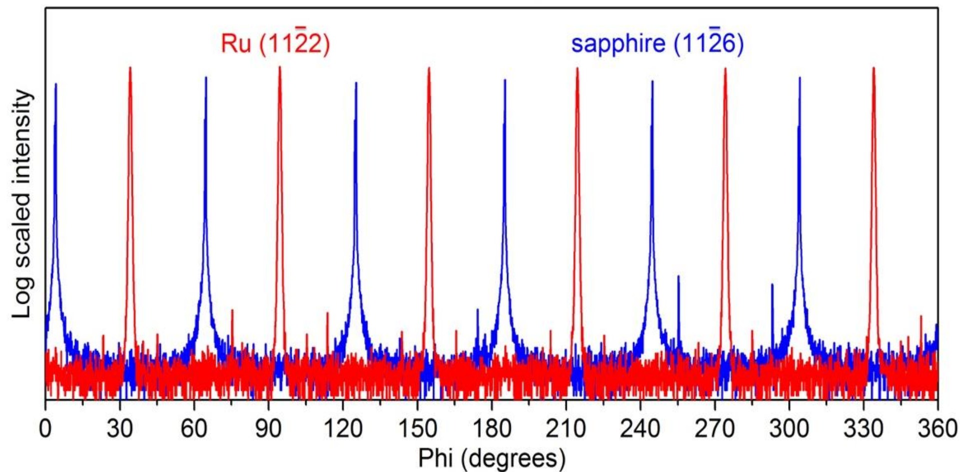

Figure 4-3 XRD ϕ scan of the Ru $\{11\bar{2}2\}$ peaks overlaid with a scan of the sapphire $\{11\bar{2}6\}$ peaks.

A 30° offset in the phi positions of these peaks was observed as expected for the 30° rotational honeycomb epitaxial relationship of (0001) Ru || (0001) sapphire and $<11\bar{2}0>$Ru $||<10\bar{1}0>$ sapphire that has been previously reported [71,82].

4.2 X-ray reflectivity

An example of the XRR experimental data and corresponding model fit is shown in Figure 4-4. The Ru layer thicknesses obtained from modeling this data are used with the sheet resistance measurements to calculate sample resistivity. It should be noted that the very thin (~ 0.2 nm or less) RuO_2 layers resulting from this modeling of XRR data may represent a physiosorbed gas layer and/or a short wavelength roughness of the Ru metal surface, rather than a distinct oxide layer.

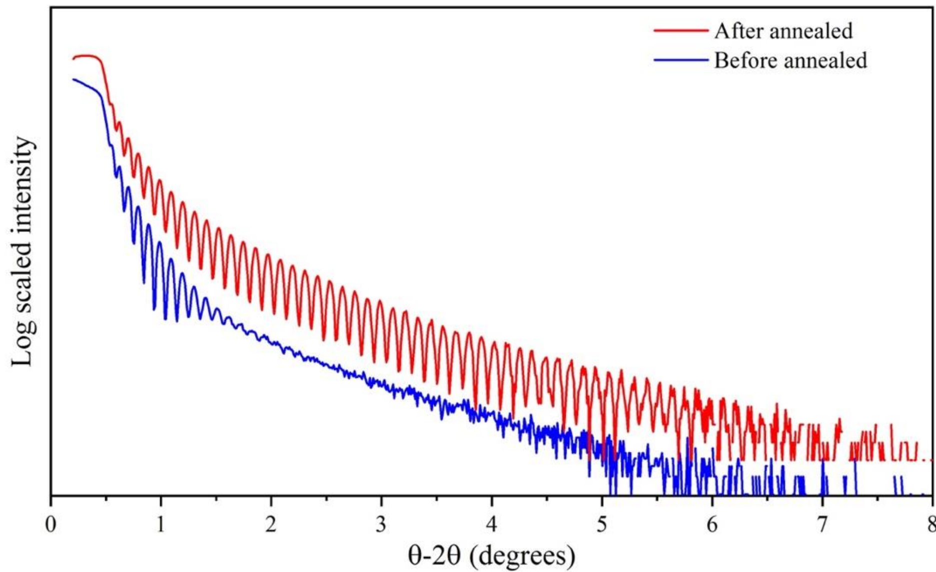

Figure 4-4 XRR data from 40 nm-thick Ru (0001) layer deposited at 400°C. (a) upper (red) curve is Ru after annealed and shifted by a factor of 10 for clarity and (b) the lower (blue) curve is the same Ru film sample before annealing (as deposited).

4.3 Roughness sample series one

The roughness of Ru samples series one was measured for Ru thin films as deposited at different temperatures and after being annealed at 700°C in one atmosphere of flowing Ar/H_2 3%. The roughness of the Ru thin films decreased after annealing as shown in Table 3-2. This decrease in roughness is expected for (0001) single crystal Ru films as it provides for a lower energy of the surface. Figure 4-5 shows the roughness of Ru thin films series one, as deposited and after annealed.

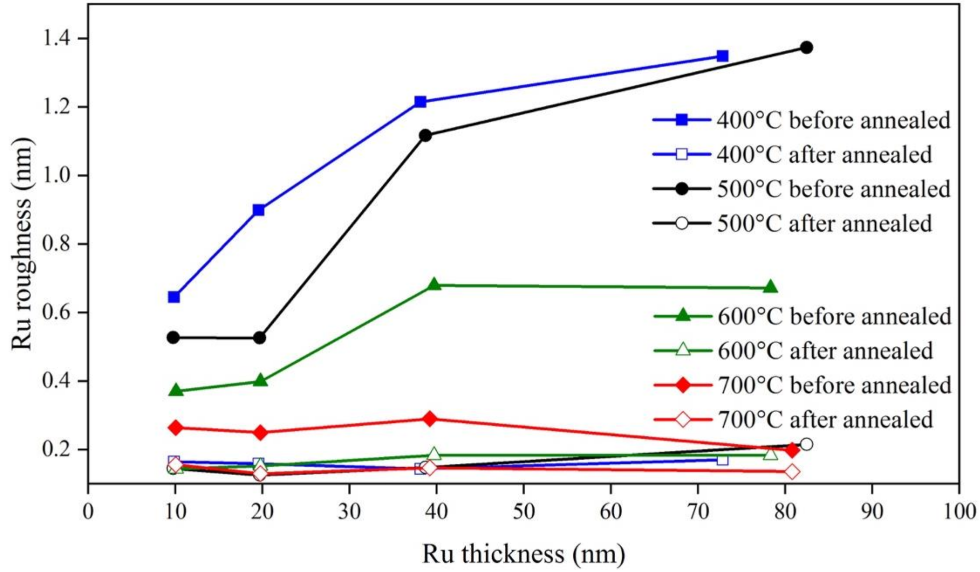

Figure 4-5 Ru roughness of Ru thin films, as deposited and after annealed.

4.4 Modelling

The influence of the thickness of a Ru film and the influence of its surface characteristics upon the resistivity of the film can be described by the Fuchs-Sondheimer (FS) model of surface scattering [29, 30], given in a simplified version [32,83] by the equation below:

$$\rho_{FS} = \rho_o \left[1 + \left[\frac{3}{8}\frac{\lambda(1-p)}{h}\right]\right] \quad (4\text{-}1)$$

where ρ_{FS} is the film resistivity, ρ_0 is the thick film resistivity of the material (absent of a surface scattering contribution), λ is the electron mean free path for scattering in thick films, p is the average of the specular scattering coefficients (probabilities) of the upper (p_u) and lower (p_l) surfaces of the film, [51] and h is the thickness of the film. In this model, changes in resistivity for a common material and constant thickness are associated with changes in the surface scattering specularity, p.

From inspection, is it clear that λ and p can be varied over a range of values and not result in a change to the model's prediction of resistivity versus thickness (ρ_{FS} versus h), as long as the product of (1-p) and λ is maintained constant, i.e. they cannot be uniquely determined by fitting to experimental data, only this product is determined. Given a value chosen for λ, then the average value of p can be determined from the experimental fitting (for example as p = 50%), but this is still not unique as this may be interpreted as both upper and lower surfaces having a 50% probability of specular reflection, or as one surface having a 0% probability and the other having a 100% probability of specular reflection of electrons [83]. The assumption of fully diffuse surface scattering from both upper and lower surfaces (p = 0%), is often made in the interpretation of experimentally measured results, particularly for studies of Cu films and lines [47]. In this work, we will study variations of resistivity as a result of changes in surface scattering, and, hence, will need a range of specularity values to correspond to the range of resistivity observed. In this case we will necessarily deviate from the p = 0% assumption.

4.5 Resistivity

4.5.1 Resistivity sample series 1

Figure 4-5 shows the resistivity associated with the variation in film thickness for sample series one, deposited at 400°C, 500°C, 600°C and 700°C, respectively. These resistivity measurements were first made after Ru deposition and ambient lab air exposure and repeated after an Ar/H_2 3% anneal to 700°C. For both measurements, thinner samples have higher resistivity than thicker, and samples prepared at lower deposition temperatures have higher resistivity than those deposited at higher temperatures. The drop in resistivity after annealing in Ar/H_2 3% anneal

to 700°C is coincident with the decrease in surface roughness but can more reasonably be attributed to a reduction in defects within the film. Figure 4-6 shows these resistivity data for series 1.

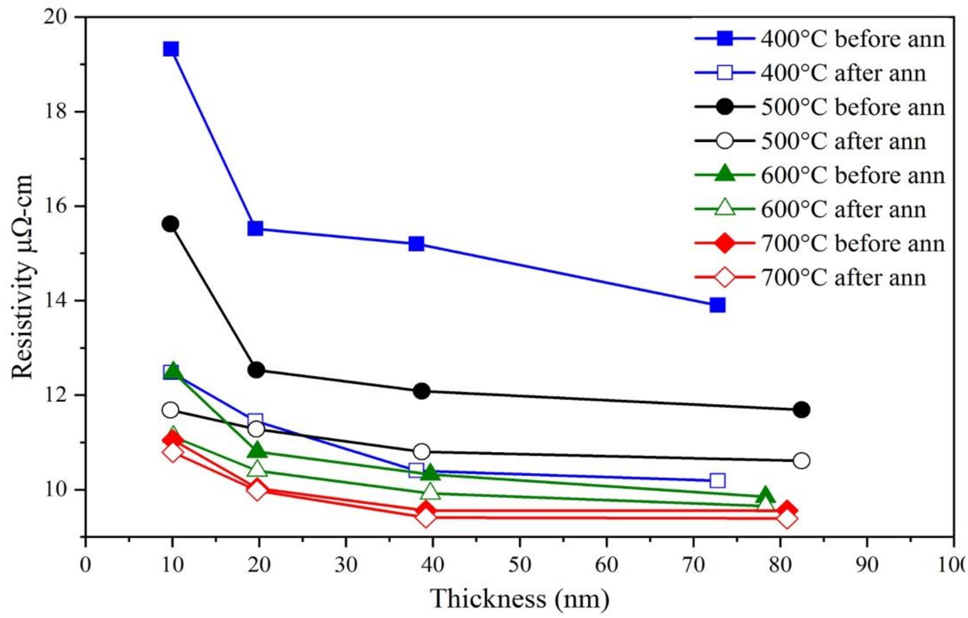

Figure 4-6 Resistivity of Ru thin films as deposited and after annealed at 700°C.

4.5.2 Resistivity sample series 2 and 3

Figure 4-7 shows the resistivity associated with the variation in film thickness for sample series 2 and 3, deposited at 350°C and 700°C, respectively. These resistivity measurements were made after Ru deposition, ambient lab air exposure, and an Ar/H_2 3% step anneal to 950°C. This higher temperature anneal was found to further reduce sample resistivity. The lower deposition temperature of 350°C was found useful to provide thinner films without dewetting during the subsequent 950°C step annealing process while slightly lower resistivity values are observed for the films deposited at 700°C. The resistivity versus thickness trends of both sample series two and three are similar and can be described with a single set of FS model parameters. Recently, it was

proposed to use a λ of 6.7 nm in a report for similar (0001) Ru films prepared in UHV conditions wherein the resistivity increase with thickness of their films was described using FS model parameters of p_o = 7.6 μΩ-cm, p = 0% and λ = 6.7 nm [71].

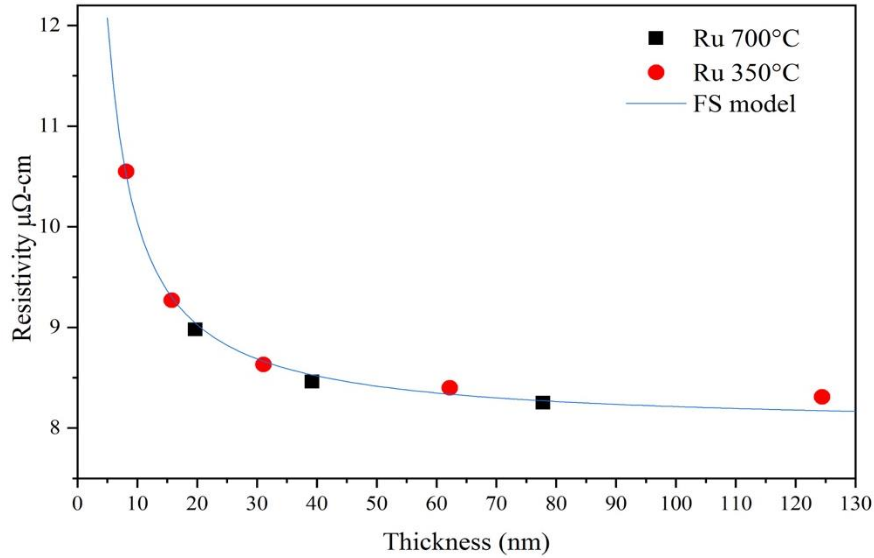

Figure 4-0-7 Resistivity versus thickness for c-axis single crystal Ru films deposited at 350°C (circles) and 700°C (squares) and ex-situ step-annealed to 950°C in Ar/H_2 3%. The solid line is the calculation of the FS model.

Using the same p of 6.7 nm, the least squares fitting of the combined data for series two and three resulted in FS model parameters of p_o = 8.0 μΩ-cm, p = 0% and λ = 6.7 nm. This is shown as the solid line if Figure 4-7 for comparison to the experimental data. Using this EMFP we find a similar result of fully diffuse surface scattering, but a slightly higher thick-film resistivity value 8.0 μΩ-cm than the prior publication. The thick film resistivity modeled is intermediate to that reported for a-plane resistivities of 7.5 and 8.2 μΩ-cm in bulk single crystal Ru samples [84-86].

4.5.3 Sample series 3

Experimental characterization data of the 8 samples of the third sample series are summarized in Table 3-3 along with the identification of the process steps after which the data was taken and the overall sequence of the process steps. A total of 8 samples were annealed together in a cumulative processing (at different temperatures in 700°C in Ar + H_2 3%, 950°C in Ar + H_2 3%, 300°C in Ar + H_2 3% and air at one atmosphere) and after each process step one sample was removed from the group for characterization. The resistivity values shown were calculated from the sheet resistance measured for each sample shown in figure 4-8 and the Ru metal layer thickness for each sample. The simple trend readily apparent in the table 3-3 is for the resistivity to decrease as a result of a reducing anneal and to increase as the result of an oxidizing anneal. Figure 4-8 shows the resistivity changes resulting from each processing step.

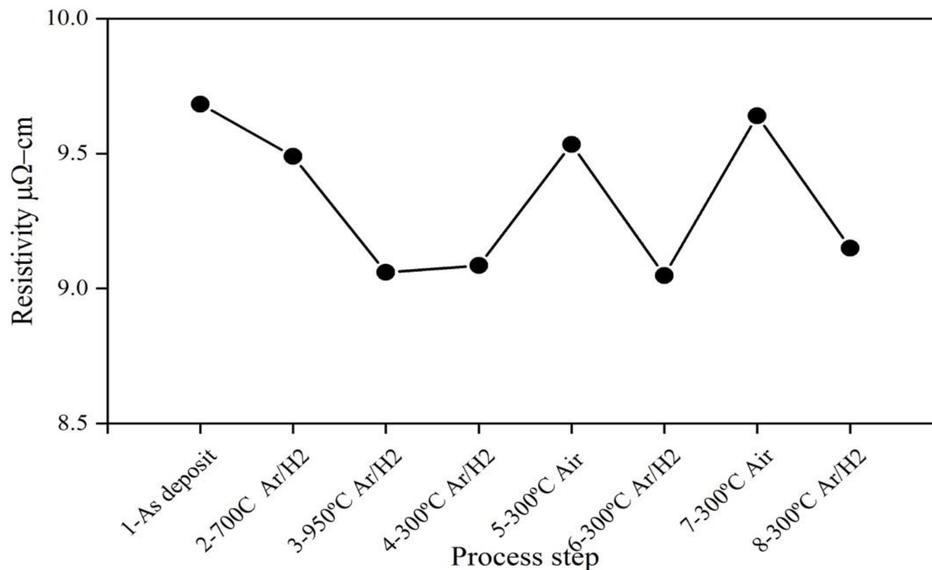

Figure 4-8 Resistivity of Ru 20 nm thin film during the annealing process

4.6 LEED characterization

The LEED characterization of the films also confirms their single crystal nature. Figure 4-8 provides LEED images from selected Ru films. Figure 4-8d is of a Ru film whose surface was cleaned by Ar ion beam sputtering and annealing in a H_2 background in the UHV system used for LEED image acquisition. This image clearly displays the six-fold symmetry expected of the single crystal Ru (0001) surface. Images 4-8a to 4-8c were obtained from air exposed Ru film surfaces without any in-situ UHV cleaning or annealing. Figure 4-8c is of a 20 nm-thick sample, deposited at 700°C, lab air exposed, and step annealed to 950°C in Ar/H_2 3% and imaged without the surface being cleaned, annealed, or prepared in any way other than by introduction to the ultra-high vacuum chamber. Notably, the six-fold symmetry expected of the Ru (0001) surface is present and qualitatively similar to that of Figure 4-9d.

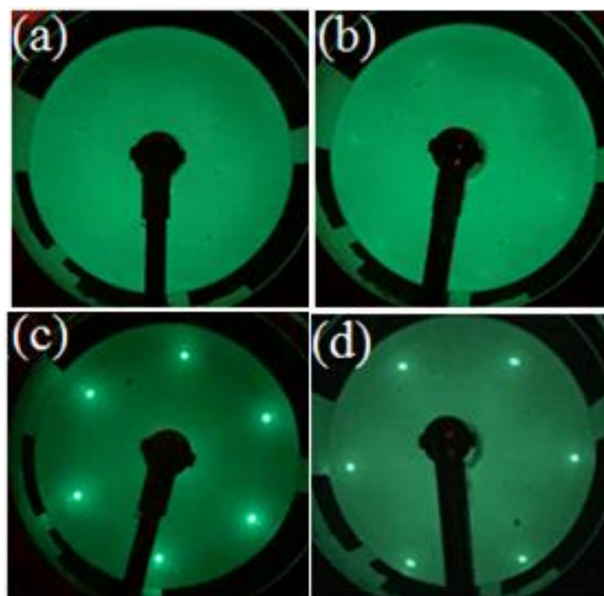

Figure 4-9 LEED images at 68 eV for an air exposed Ru film (a) after deposition at 350°C, (b) after deposition at 700°C, (c) after deposition at 700°C and ex-situ annealing to 950°C in Ar/3%H_2, and (d) a sample Ar ion beam cleaned and annealed to 1,000°C in UHV conditions with an H_2 background.

While it is not clear if the LEED image of Figures 4-9a to 4-9c are the result of low energy electrons reflecting from the Ru atoms directly, or from an absorbed gas layer on the Ru surface, it is clear that an ordered surface structure is, surprisingly, observable after the exposure of the Ru film to ambient air. This also indicates that a relatively well atomically ordered Ru (0001) surface resulted from the deposition and ex-situ 950°C Ar/H_2 3% anneal processing of the Ru single crystal films and that this high degree of atomic surface order persists during laboratory air exposure. Figures 3a and 3b are from samples as deposited at 350°C and 700°C, respectively, and imaged without the 950°C Ar/H_2 3% anneal. A qualitatively weaker six-fold pattern is present in Figure 4-9b and is essentially absent in Figure 4-9a.

In this dissertation, the additional modifications to the surfaces of samples in series 4, 5, and 6, prepared identically to those of series 3, result in increases in film resistivity. This cannot be accommodated by a set of FS model parameters that has the Ru surfaces already fully diffuse ($p = 0\%$). A larger λ value is needed to allow variations in specularity (i.e., $100\% > p > 0\%$) while maintaining the product, $(1\text{-}p)\ \lambda = 6.7$ nm, constant to be consistent with the data and fitting of Figure 4-7. Table 4-1 lists some of the possible alternative assumptions of FS model parameters that maintain this product constant. While every set of model parameters shown in Table 4-1 can equally provide the FS prediction shown in Figure 4-7, we choose to use the set of $\rho_o = 8.0$ μΩ-cm, $\lambda = 11$ nm, and $p_l = 0\%$ and $p_u = 78\%$ as these provide for variations of resistivity associated with changes to the upper Ru surface while avoiding large values for the λ that are inconsistent with the previous work.

The high specularity $p_u = 78\%$, of the air-exposed Ru surface is surprising in light of prior UHV experiments for single crystal Ni and Cu surfaces where ambient air and sub-monolayer gas

exposure were found to induce fully diffuse scattering [47]. However, the high specularity of the top Ru surface is consistent with the air-exposure stability of the highly ordered surface structure of these films evidenced in the LEED images of Figure 4-9, and is also consistent with the report of no increase in the resistivity of similar single crystal Ru samples measured ex-situ as compared to their resistivity measured in-situ after deposition and annealing in ultra-high vacuum conditions [71].

Table 4-1 Listing of FS model parameters

EMFP λ, nm	Thick Film Resistivity ρ_o, μΩ-cm	Average Surface Specularity, p	Upper Surface Specularity p_U	Lower Surface Specularity p_L
6.7	8.0	0%	0%	0%
11.0	8.0	39%	39%	39%
11.0	8.0	39%	78%	0%
30.8	8.0	39%	78%	78%

The (0001) surfaces of single crystal Ru thin films ex-situ annealed at 950°C in Ar + H_2 3% were found to form a highly ordered atomic surface structure that was stable to subsequent air exposure, as evidenced by LEED. Films with this structure for the upper Ru surface were found to have a relatively low resistivity that was correlated to a relatively high specular scattering probability, i.e., largely specular surface, for the upper surface in the context of the FS semi-classical model of the resistivity size effect.

4.7 XPS characterization Ru

The chemistry of the film surface was studied by XPS, collected under ultra-high vacuum (base pressure ~ 5 x 10^{-10} Torr) conditions using a SPECS Electron Spectrometer with a PHOIBOS 100

Hemispherical Energy Analyzer and XR 50 Al K_{α} X-ray source (1486.67 eV). The XPS spectra were collected at a pass energy of 20 eV with energy resolution of 0.1 eV. The XPS spectra were fitted using XPSPEAK 4.1 program with Gaussian/Lorentzian mixed peak shape and with Shirley background correction. The normalized Ru $3d_{5/2}$ peak heights allowed interpretation by fitting to two components, Ru^0 and oxidized $Ru^{\delta+}$, at binding energies (BEs) consistent with metallic Ru and RuO_2, respectively. In addition, C 1s features have also been included as needed to fit the data.

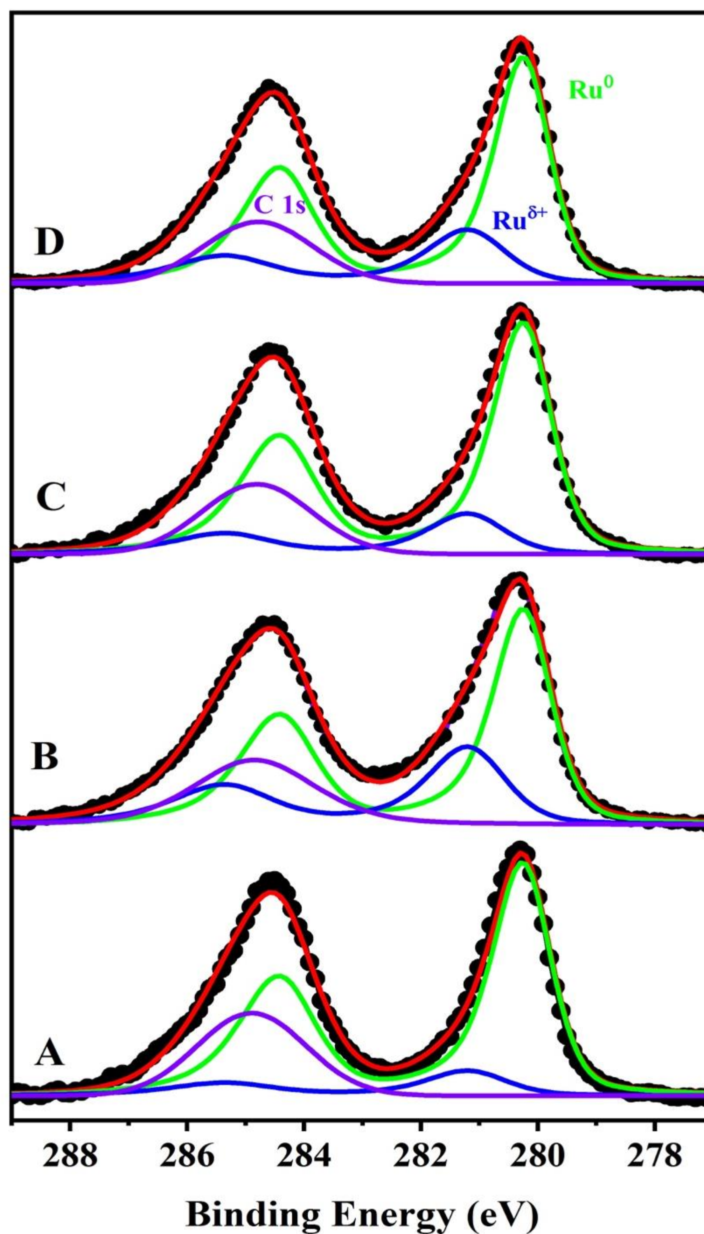

Figure 4-10 Represents a series of XPS spectra of Ru 3d peak collected from samples annealing in two different environments, Ar/H_2 and air, alternatively. Samples A and C are after annealed in Ar/H_2 (3%) atmosphere where samples B and D after annealed in air at 300C.

To generate the fits, an empirical line shape for the metallic Ru (Ru^0) was established, using a rigorously cleaned Ru (0001) single-crystal kept within the vacuum system. With the shape, width,

and position of this peak constrained to fixed values equivalent to those from the control sample, a second peak associated with RuO_2 ($Ru^{\delta+}$) was added to the experimental spectra of each sample as needed to ensure proper fitting of the 5/2 spin-orbit splitting components, where the C 1s signal is not expected to contribute to the XPS intensity. With the 5/2 component fit as well as possible by the two features associated with oxidized and unoxidized Ru, residual differences between the data and the fitting in the Ru 3d 3/2 component region of the spectra, the higher binding energy (BE) feature present in each, were fit to a single unconstrained C 1s peak. From XPS spectra it is clear that the oxide component ($Ru^{\delta+}$) of Ru 3d increased after annealing in air (Figure 4-9b, and 4-9d) and it decreases in more reducing environment (Ar/H_2).

CHAPTER 5 Ru/SiO_2 and Ru/Al_2O_3 INTERFACE

5.1 XRR layer thickness

An example of the XRR experimental data and corresponding model fit is shown in Figure 5-1 for a Ru film sample overcoated with SiO_2. The obvious higher frequency oscillations correspond to the Ru film thickness of 20 nm. Also present are superimposed weaker, longer wavelength oscillations associated with the 5 nm SiO_2 overlayer. The Ru and SiO_2 layer thicknesses are obtained from modeling this data and the former is used with the sheet resistance measurements to calculate sample resistivity. For sample series 5, XRR characterization was performed at each processing step on each sample coupon and these results are summarized in Table 3-2. It should be noted that the very thin (~ 0.2 nm or less) RuO_2 layers resulting from this modeling of XRR data may represent a physiosorbed gas layer and/or a short wavelength roughness of the Ru metal surface, rather than a distinct oxide layer.

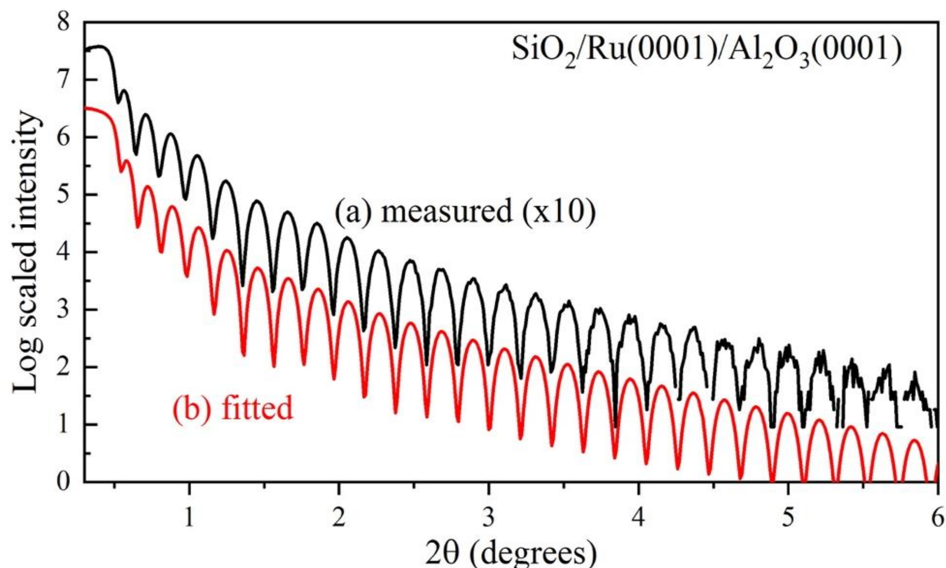

Figure 5-1 XRR data from a 4.6nm thick SiO_2 on a 20.8nm-thick Ru (0001) layer. (a) upper (black) curve is for measured data shifted by a factor of 10 for clarity and (b) the lower (red) curve is the model prediction.

5.2 XPS characterization Ru/SiO_2

The chemistry of the film surface and Ru/SiO_2 interfacial region was studied by XPS, collected under ultra-high vacuum (base pressure ~ 5 x 10^{-10} Torr) conditions using a SPECS Electron Spectrometer with a PHOIBOS 100 Hemispherical Energy Analyzer and XR 50 Al K_α X-ray source (1486.67 eV). An example of the XPS characterization is shown in Figure 5-2, which shows representative XPS data taken from the same sample at three different steps along the 11-stage process shown in Table 3-2 for sample series 5. The XPS spectra were collected at a pass energy of 20 eV with energy resolution of 0.1 eV. The XPS spectra were fitted using XPSPEAK 4.1 program with Gaussian/Lorentzian mixed peak shape and with Shirley background correction. The normalized Ru $3d_{5/2}$ peak heights allowed interpretation by fitting to two components, Ru^0 and oxidized $Ru^{\delta+}$, at binding energies (BEs) consistent with metallic Ru and RuO_2, respectively.

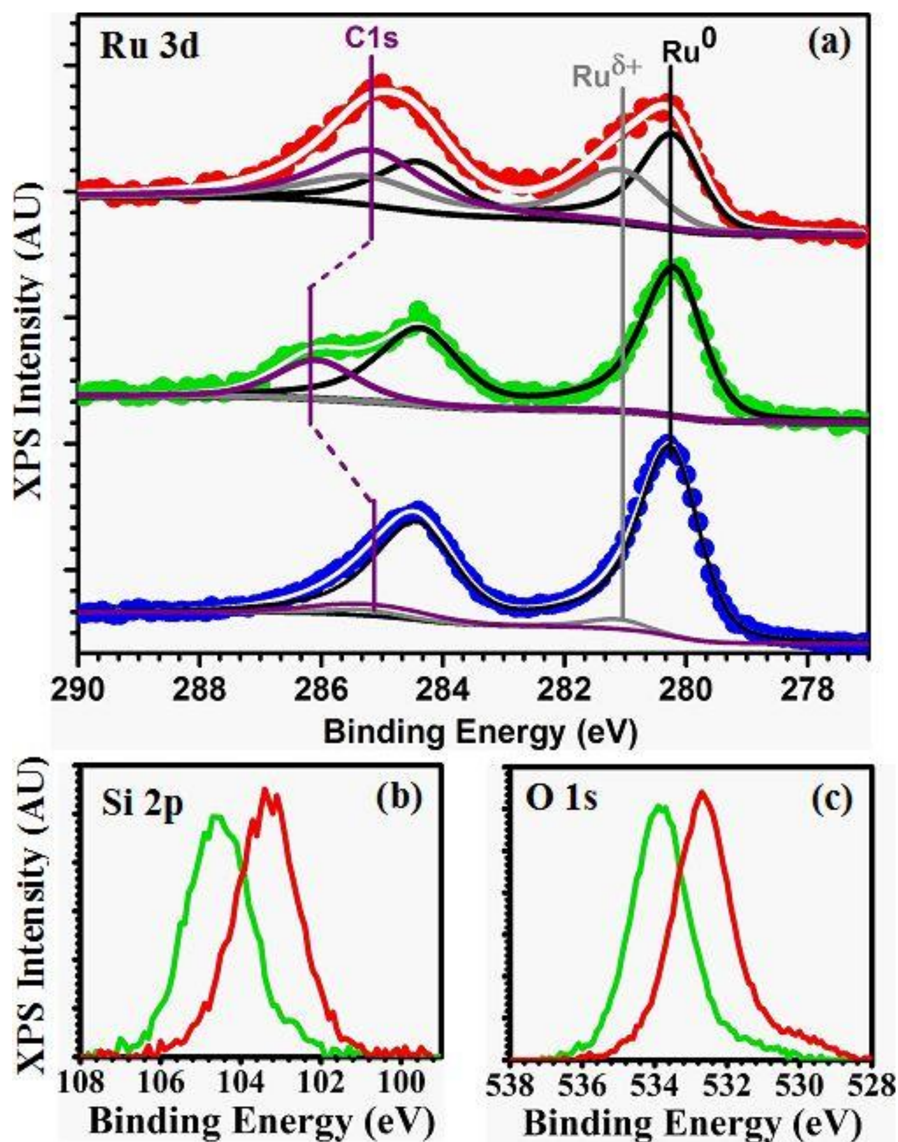

Figure 5-2 XPS data for Ru 3d (a), Si 2p (b), and O 1s (c) for the same sample following the 2nd (blue) 4th (green), and 5th (red) stage in the annealing process described in Table 3-2. Ru^{0} and $Ru^{\delta+}$ in figure 5-2(a) correspond to metallic ruthenium and ruthenium oxide (RuO_2) respectively.

In addition, C 1s features have also been included as needed to fit the data, and angle-dependent measurements (not shown) have been employed to confirm the enhanced surface preference of the C and $Ru^{\delta+}$ species relative to Ru^{0} in select samples. To generate the fits, an empirical line shape

for the metallic Ru (Ru^0) was established, using a rigorously cleaned Ru (0001) single-crystal kept within the vacuum system. With the shape, width, and position of this peak constrained to fixed values equivalent to those from the control sample, a second peak associated with RuO_2 ($Ru^{\delta+}$) was added to the experimental spectra of each sample as needed to ensure proper fitting of the 5/2 spin-orbit splitting components, where the C 1s signal is not expected to contribute to the XPS intensity. With the 5/2 component fit as well as possible by the two features associated with oxidized and unoxidized Ru, residual differences between the data and the fitting in the Ru 3d 3/2 component region of the spectra, the higher binding energy (BE) feature present in each, were fit to a single unconstrained C 1s peak.

Noting large variations in both the position and intensity of the C 1s features needed to accurately fit our data as a function of condition, we obtained XPS spectra associated with step 7 for two samples exposed to air for drastically different periods of time between annealing and vacuum introduction, which was an uncontrolled (but measured) variable throughout the remainder of the data set. This variable results in clear changes to the amount of C detected by XPS, but does not result in changes to the $Ru^{\delta+}$:Ru^0 XPS intensity ratio. To provide further insight into the nature of the spurious carbon species on the samples, we also provide O 1s and Si 2p regional XPS plots from the 4th and 5th process steps in Figure 5-2. Interestingly, the same ~1 eV shift to lower binding energy (BE) noted for the C 1s contribution to the Ru 3d region is also noted in both the O 1s and Si 2p data when transitioning from step 4 (Ar/H_2 annealing) to step 5 (air annealing) in our multi-step process sequence. This combination of data is consistent with carbon on or within the SiO_2 layer present at the interface of Ru undergoing changes in work-function as the interfacial oxidation state of the metal transitions from Ru to RuO_2, which then results in

equivalent band-bending shifts to the BEs associated with all elements present within the insulating oxide layer. Since oxidation is known to increase the work-function of Ru, band-bending effects near the surface are expected to concomitantly decrease the BE of core-levels in the supported oxide when oxidizing the Ru metal. Similar rationalizations have been used to explain core-level shifts observed in other Ru-supported, silicate thin-films following the deliberate intercalation of a number of atomic species, such as: O, Au, Pd, and Cu [87,88].

5.3 LEED of Ru/SiO_2 and Ru/Al_2O_3

A LEED image from a sample overcoated with 5 nm of SiO2 on Ru/SiO_2 or 6 nm of Al_2O_3 on Ru/ Al_2O_3 were obtained and, as expected, no spot pattern was present due to the amorphous nature of the SiO_2 and Al_2O_3 layers. Figure 5-3a for Ru/SiO_2 and 5-3b Ru/ Al_2O_3 shows the LEED images.

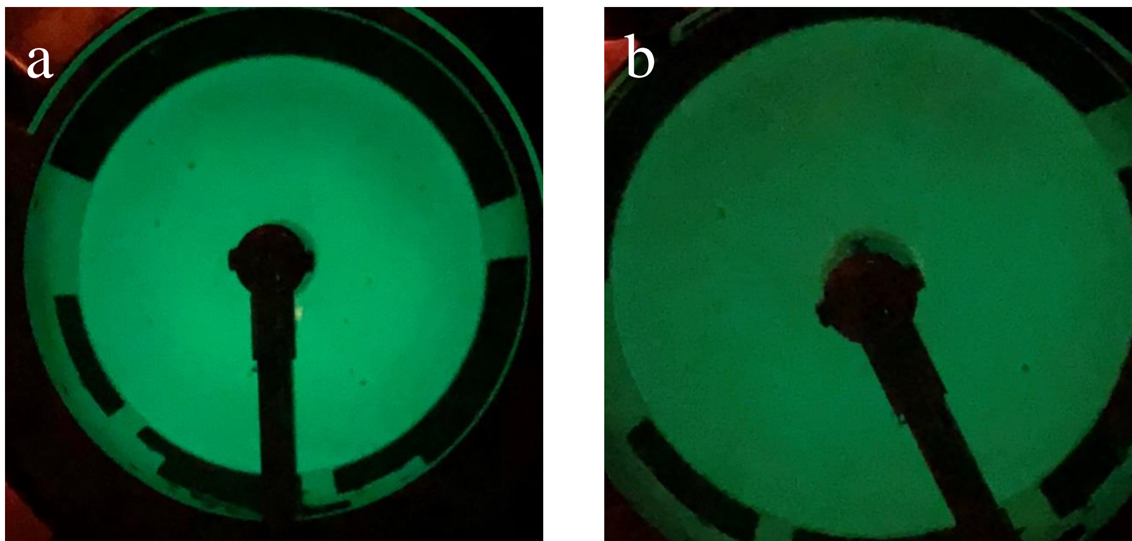

Figure 5-3 LEED images at 68 eV for an air exposed (a) Ru/SiO_2 and (b) Ru/Al_2O_3

5.4 Resistivity and specularity

5.4.1 Sample series 4 - evaporated SiO_2 on Ru 20 nm films

The fourth sample series explored the effect of UHV evaporation of SiO_2 on coupons having 20 nm-thick Ru films that had been step annealed to 950°. One sample from the wafer was not overcoated (0 nm) to allow comparison of resistivities, one was coated with 0.5 nm, and two coupons were overcoated with 5 nm and another two with 30 nm of SiO_2. Figure 4-7 shows the increase in resistivity and the drop in upper surface specularity, p_u, associated with the UHV evaporation of SiO_2 onto the sample surface. The error bars shown in Figure 4-7 reflect the estimated error in thicknesses of the individual coupons in the absence of individual XRR characterization of each (only the full as-deposited wafer was measured).

It is clear that even the thinnest SiO_2 deposit of 0.5 nm results in an increase in resistivity that can only be accounted for by an increase in diffuse scattering of the upper Ru metal surface, as this low energy deposition at room temperature cannot be responsible for changes in defects within the Ru layer. We conclude that the specularity and surface order present after the 950°C step anneal in Ar + H_2 3% (e.g., as evidenced in Figure 4-7c) is degraded by the SiO_2 deposition, which brings reactive Si and O adatoms and SiO_x molecules to the sample surface, and apparently is more disruptive to specular scattering than the ambient air exposure of predominantly stable gaseous species (N_2, O_2, others). The upper surface specularity change is shown in Figure 4-7 as well, using the FS model with $\rho_o = 8.0$ μΩ-cm, $\lambda = 11$ nm, and $p_l = 0\%$. The increase in resistance and decrease in specularity is associated only with changes in the specularity of the upper Ru surface as the room temperature SiO_2 deposition is not expected to change scattering within the Ru layer or scattering at the lower Ru/sapphire interface.

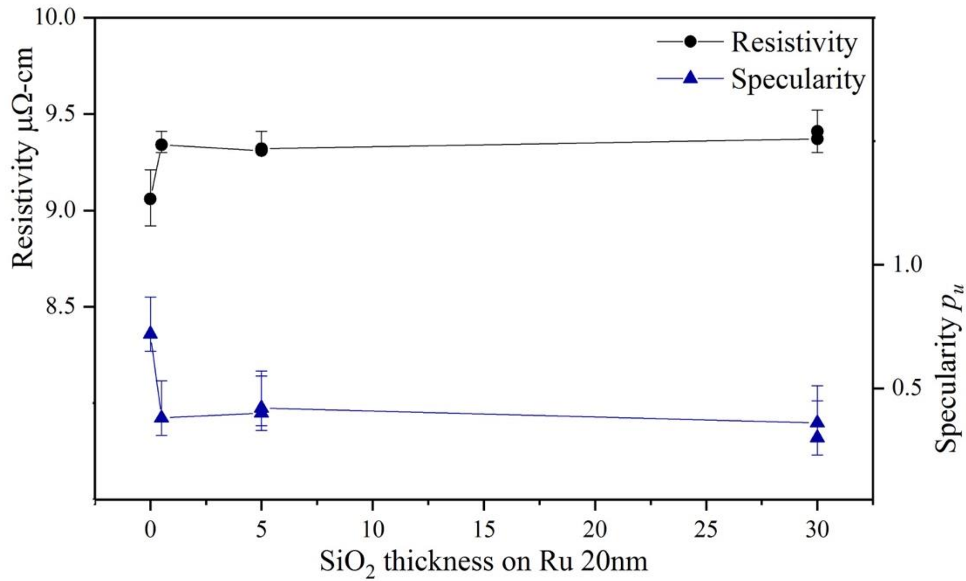

Figure 5-4 Resistivity and calculated upper surface specularity for the FS model as a function of evaporated SiO_2 thickness for 20 nm thick Ru samples.

5.4.2 Sample series 5 - sputtered SiO_2 on Ru 20 nm films

Experimental characterization data of the five samples of the fifth sample series are summarized in Table 3-4 along with the identification of the process steps after which the data was taken and the overall sequence of the process steps. It should be noted that the five samples were subjected simultaneously to all of the processing steps shown in the table, including the sputter deposition of a single 5 nm-thick layer of SiO_2. The data from each coupon are listed in a consistent order in each cell of Table 3-4, and the minimum and maximum value of each cell is used to provide the error estimations shown in Figures 5-5 and 5-6.

The resistivity values shown were calculated from the sheet resistance measured for each sample (not shown) and the Ru metal layer thickness for each sample, both parameters measured at each process step to eliminate this source of variability (shown as the error bars in Figure 5-4).

The simple trend readily apparent in the table is for the resistivity to decrease as a result of a reducing anneal and to increase as a result of the SiO_2 overlayer deposition or as the result of an oxidizing anneal.

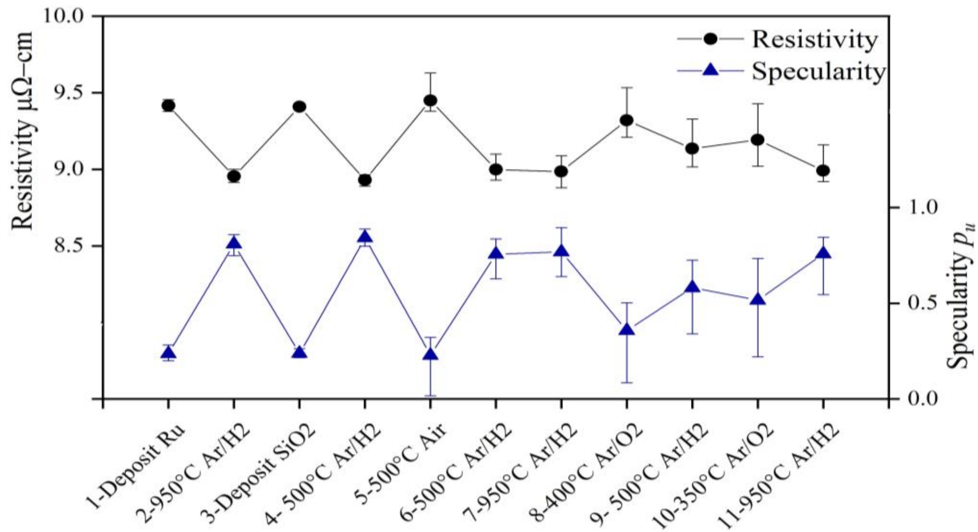

Figure 5-5 Film resistivity and FS model upper surface specularity (p_u) as a function of sample processing. Shown are average values for the five samples with error bars to reflect the extreme values amongst the five.

Figure 5-6 shows the resistivity changes (left-hand axis) resulting from each processing step. Also observed here is the increase in resistivity resulting from the deposition of an amorphous 5 nm-thick SiO_2 overlayer on top of the Ru films that had been previously step annealed to 950°C in Ar + H_2 3%. As above, these resistivity changes are described by the FS model with ρ_o = 8.0 μΩ-cm, λ = 11 nm, and p_l = 0%. As with sample series 4, an increase in surface roughness, a change in defect-related scattering within the layer, or a change in the lower Ru/sapphire interface cannot be expected from the room temperature SiO_2 overlayer deposition. The addition of the amorphous overlayer is understood to have increased surface scattering of the upper Ru surface, by an increase in the diffuse scattering fraction, from a surface that was largely specular. This

increase in diffuse scattering can be understood as resulting from localized surface states that scatter electrons [44,47]. These states are likely associated with atomic scale defects and/or the irregular bonding of Si and O adatoms and SiO_x molecules at the Ru metal surface. The variations of the specularity of the upper surface are also shown in Figure 5-6 using the right-hand axis and exhibit a variation in specularity of approximately 60%. Figure 5-6 plots the average value and presents the minimum and maximum values of the five samples as errors bars. It is evident that the difference between the maximum and minimum values in resistivity (and hence specularity) tends to increase with additional processing steps. We attribute this to the physical damage (i.e., scratches) imparted by the repeated probing of the sample surface by the sharp W wire contacts for the Van der Pauw sheet resistance measurements.

Figure 5-6 summarizes the trend of several of the measured sample characteristics from Table 3-4 as a function of processing step and compares these to the changes in FS model specularity. Shown are the changes in the Ru metal layer thickness (from the as-deposited state), the RuO_2 layer thickness, the XPS Ru^+/Ru^0 ratio, the Ru upper surface roughness, and the calculated specularity. It is evident that the oxidizing anneals, steps 5 and 8, at 500°C and 400°C respectively, provided a significant increase in the RuO_2 thickness with corresponding decreases in the Ru metal thickness that are consistent with the expected variations in stoichiometry and density in the two layers. A much weaker effect was observed for step 10, an oxidizing anneal at 350°C. The higher temperature oxidizing anneals also destroyed the relatively specular scattering of the Ru upper surface to values similar to that immediately following SiO_2 overlayer deposition.

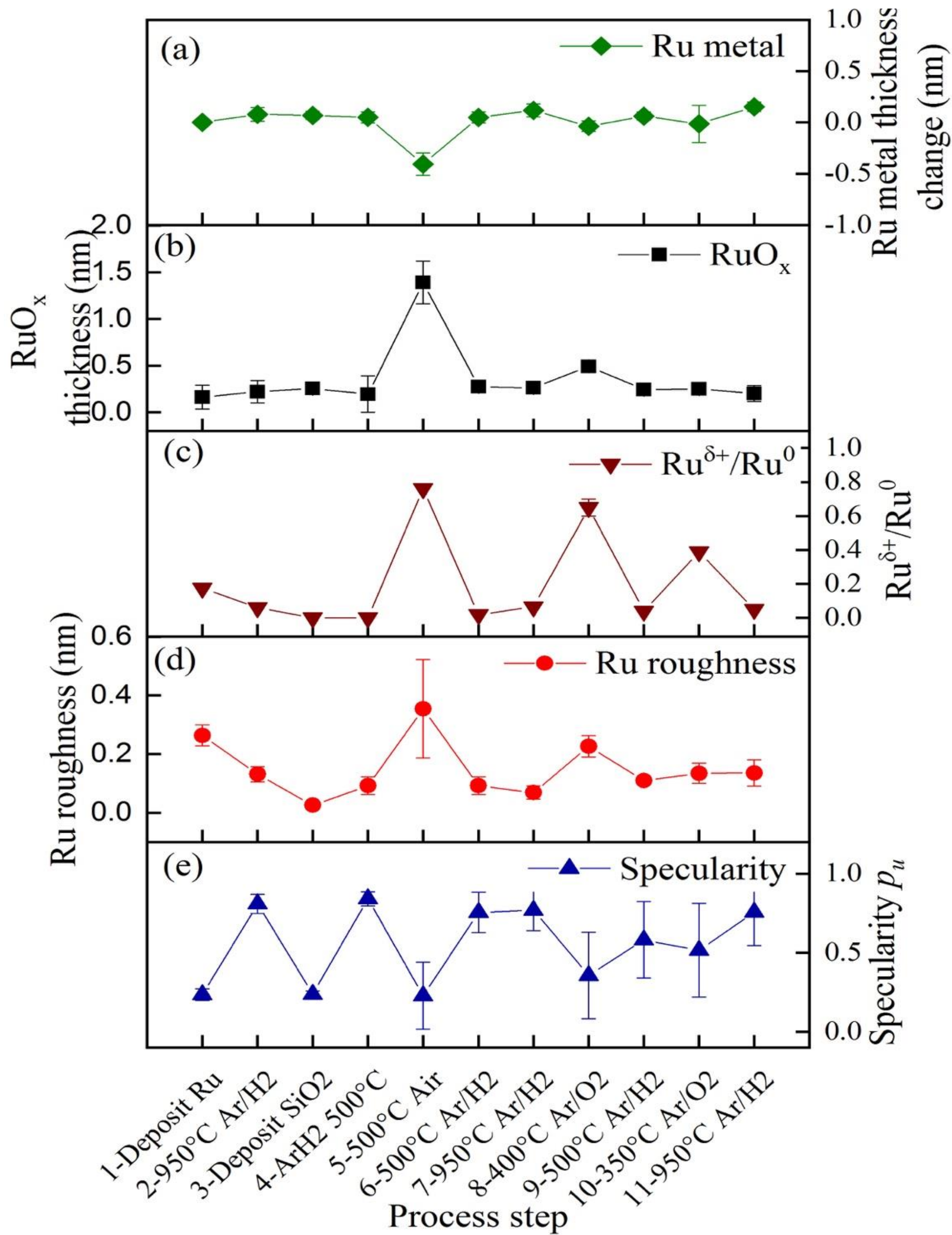

Figure 5-6 Shows (a) Ru metal thickness change, (b) RuO_x, (c) Ru oxide to Ru metal ratio, (d) Ru roughness and (e) surface specularity (*p*) processing as a function of sample shown are average values for the five samples with error bars to reflect the extreme values amongst the five.

A surprising observation is that, in all cases, the higher surface specularity immediately following the first 950°C step anneal in Ar + H_2 3% (process step 2, with surface quality as imaged in Figure 4-7c) could be restored by a subsequent Ar + H_2 3% anneal, at temperatures as low as 500°C, even with the amorphous SiO_2 overlayer present. In other words, the transition between mostly specular and mostly diffuse scattering from the upper surface was found to be reversible. The oxidizing anneals also resulted in a reversible increase in the roughness of the Ru upper surface, but these changes are small and would only account for a small fraction of the resistivity changes observed [38,71]. The comparison data between the XRR data of RuO_x layer and the XPS Ru^+/Ru^0 ratio data are shown in figure 5-7, where the data from XPS is more sensitive to oxide bond formation.

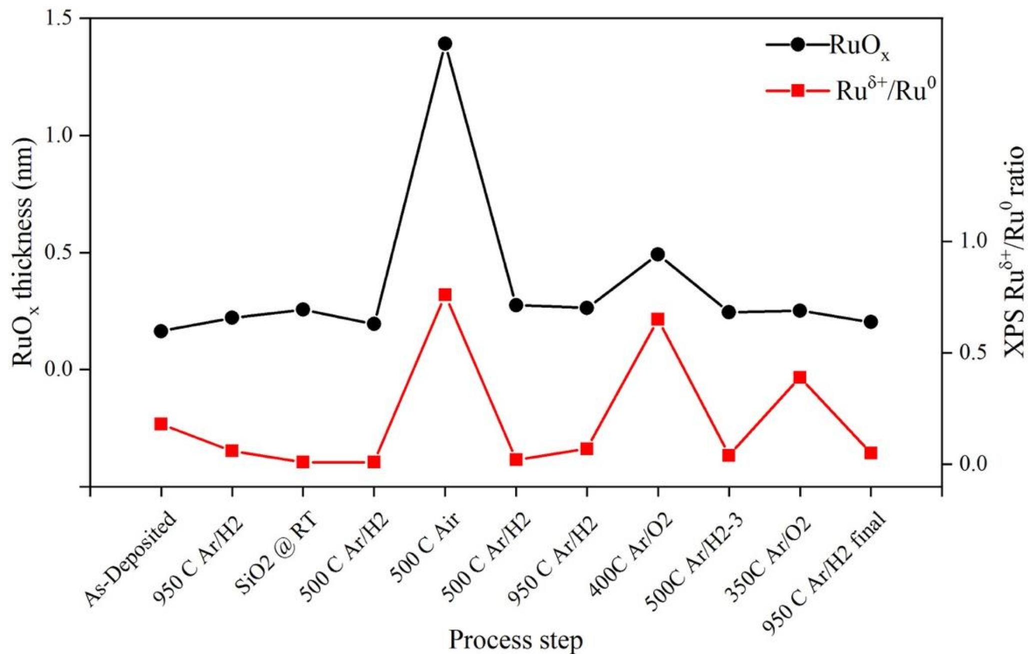

Figure 5-7 The comparison between the XRR of RuO_x layer and the XPS Ru^+/Ru^0 ratio

5.4.3 Samples series 6 - Sputtered Al_2O_3 on Ru 20 nm films

The summary of the three samples of the sixth sample series are in Table 3-5 along with the identification of the process steps after which the data was taken and the overall sequence of the process steps. It should be noted that the three samples were subjected simultaneously to all of the processing steps shown in the table, including the sputter deposition of a single 6 nm-thick layer of Al_2O_3. The data from each coupon are listed in a consistent order in each cell of Table 3-5.

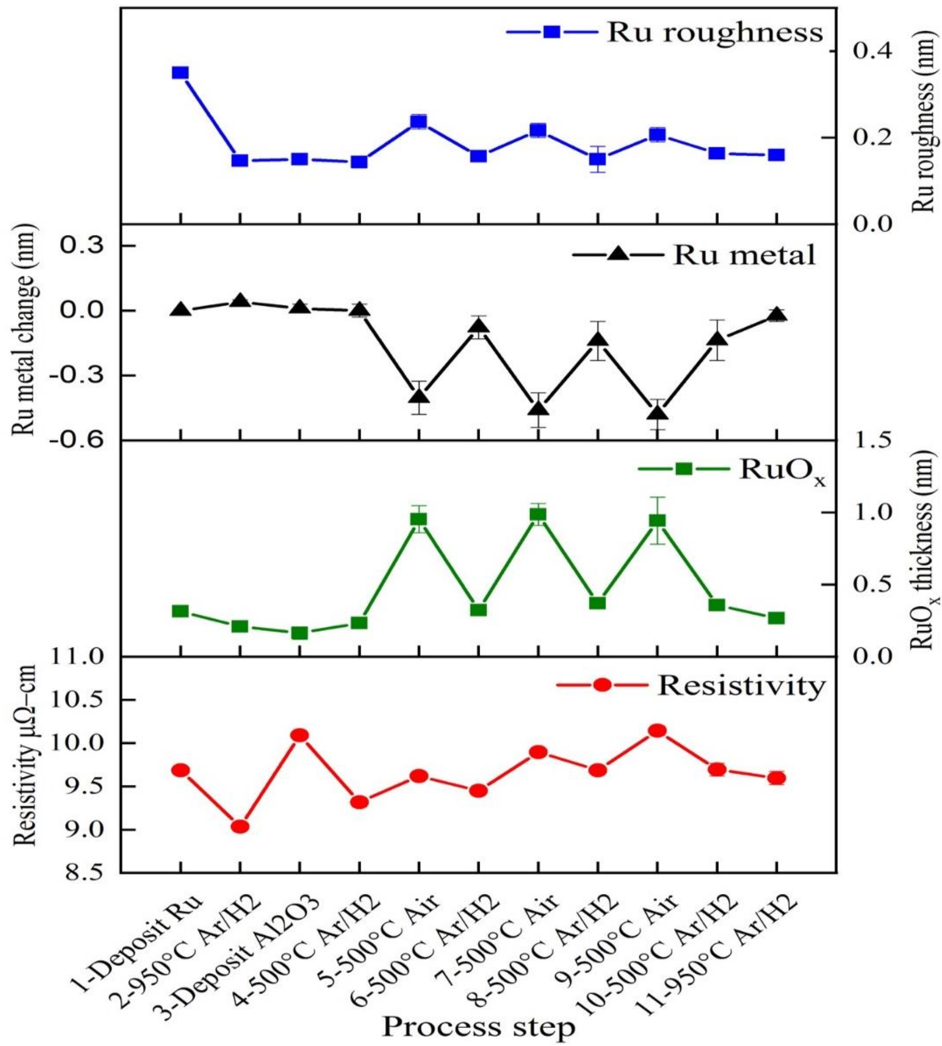

Figure 5-8 Film resistivity, RuO_x, Ru metal thickness, and roughness as a function of sample processing. Shown are average values for the three samples with error bars to reflect the extreme values amongst the three.

The resistivity values shown were calculated from the sheet resistance measured for each sample (not shown) and the Ru metal layer thickness for each sample, both parameters measured at each process step to eliminate this source of variability (shown as the error bars in Figure 5-8). The simple trend readily apparent in the table is for the resistivity to decrease as a result of a

reducing anneal and to increase as a result of the Al_2O_3 overlayer deposition or as the result of an oxidizing anneal.

Steps 5, 7, and 9, at 500°C provided a significant increase in the RuO_2 thickness with corresponding decreases in the Ru metal thickness that are consistent with the expected variations in stoichiometry and density in the two layers. The last anneal at 950°C in Ar + H_2 3% decreased the resistivity but not to the same extent as for sample series 5 where the anneal at 950°C in Ar + H_2 3% restored the samples to the initial low resistivity condition. Sample series 6 (Ru/Al_2O_3) exhibited and even greater difference between maximum and minimum resistivity and was not fit to an FS model because of the large value of λ this would have required.

CHAPTER 6 RUTHENIUM ON $(11\bar{2}0)$, $(10\bar{2}0)$, $(10\bar{1}2)$, and $(10\bar{1}4)$ SAPPHIRE

6.1 Introduction

Single crystal thin films of ruthenium on oxide substrates are expected to be important to future semiconductor interconnect technology due to its relatively lower resistivity and high melting temperature. Ruthenium has a hexagonal close-packed (hcp) crystal structure and even in bulk form has a lower electrical resistivity for current directed parallel to the crystallographic c-axis than for current in directions perpendicular to the c-axis. Of specific interest is that crystallographic planes perpendicular to the c-axis have lower surface energy and the electric current flowing parallel to the c-axis has lower resistivity The prior work allowed the formation of single crystal Ru films with the c-axis perpendicular to the film layer, which resulted in only the higher resistivity directions available for nanowire semiconductor interconnects. The structure that attempt to grow is a single crystal Ru film on an insulating substrate that has the c-axis in the plane, this will allow a significant reduction in the resistance of Ru when used for semiconductor interconnect nanowires. The Ru thin films were deposited on different sapphire substrate such as sapphire $(11\bar{2}0)$, $(10\bar{1}0)$, $(10\bar{1}2)$, and $(10\bar{1}4)$ substrate. These depositions were an attempt to grow a single crystal c-axis in the plane on these sapphire substrates.

6.2 Ru on sapphire $(11\bar{2}0)$

Ru 40 nm thin films were deposited on $(11\bar{2}0)$ oriented sapphire single crystals at temperatures of 500°C, 550°C, 600°C, and 650°C. The preparation process of these thin films has been otherwise described in section 3.5.1. These depositions were an attempt to grow a single crystal $(10\bar{1}0)$ oriented Ru film on the sapphire $(11\bar{2}0)$ substrate, as it is known that c-axis epitaxy with this 30 degree relative rotation of unit cells is possible. However, while in these experiments a nearly single crystal film of Ru was grown, the films had a c-axis, (0001), orientation.

This is evident in Figure 6-1 which shows only the specular X-ray diffraction $(11\bar{2}0)$ sapphire peak and Ru (0002) peak.

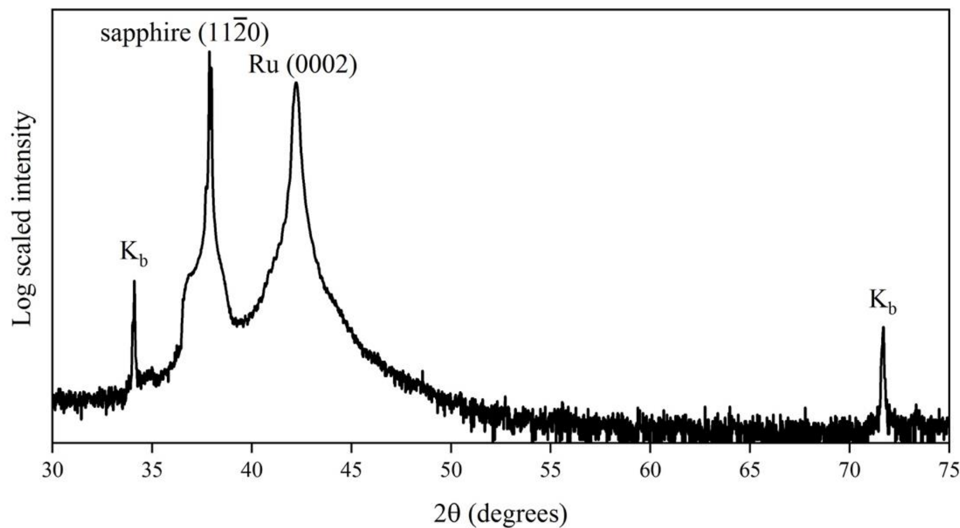

Figure 6-1 XRD for a Ru film on sapphire $(11\bar{2}0)$ deposited at 500ºC with thickness d = 39.7 nm

The "nearly single crystal" nature of the films was evident in the phi (ϕ) scan for the film deposited at 600°C shown if Figure 6.2. This shows two sets of six $(10\bar{1}0)$ peaks (at θ= 22.0075° , 2θ = 44.015°, and c = 61.31°) for the Ru film that are 30 degrees offset from each other.

A (0001) textured Ru film (c-axis perpendicular to the substrate plane) that was polycrystalline and randomly oriented in the plane of the film would have no peaks, just a uniform intensity, while a single crystal film would have just a single set of six peaks. The second set of six peaks indicates that the film has two different epitaxial orientations to the substrate and hence is not single crystalline. Unfortunately, there was no indication of the Ru $(10\bar{1}0)$ orientation that was desired for the sapphire $(11\bar{2}0)$.

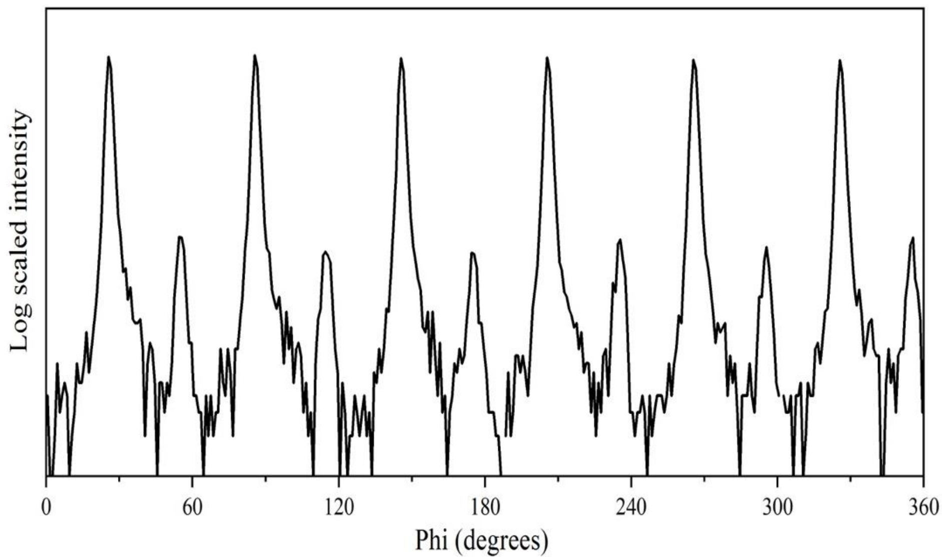

Figure 6-2 The ϕ scan of Ru thin film on sapphire $(11\bar{2}0)$

The single crystal nature of the sapphire substrate was confirmed with a ϕ scan of the sapphire $(11\bar{2}0)$ peaks wherein two peaks with 180° between them were observed, as shown in figure 6-3.

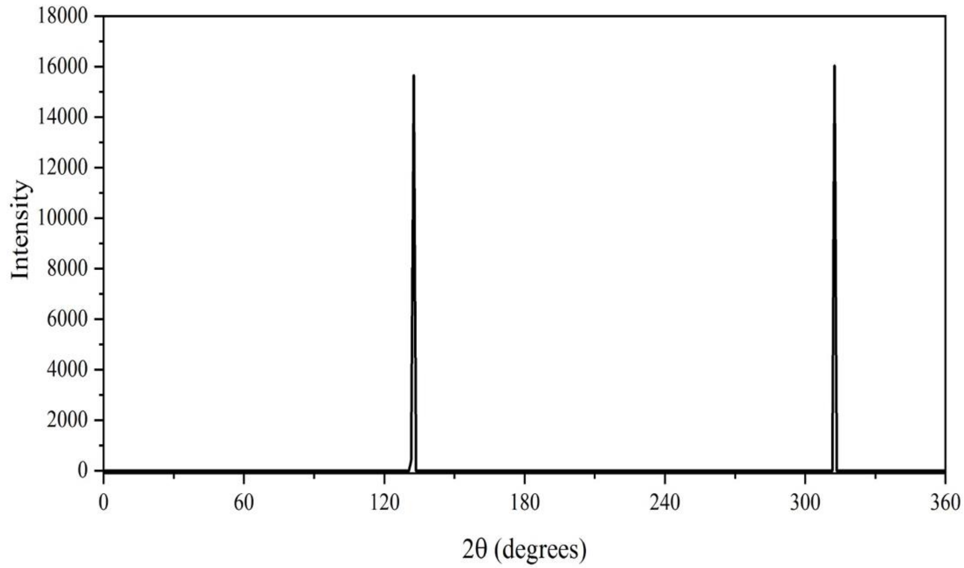

Figure 6-3 The ϕ scan of sapphire ($11\bar{2}0$)

The resistivity of these Ru thin films was higher than the Ru thin films (0001) on sapphire (0001), shown in table 6-1.

Table 6-1 The thickness, roughness, and resistivity of Ru 40 nm thin films on sapphire ($11\bar{2}0$).

Deposition temperature °C	Thickness (nm)	Roughness (nm)	Resistivity (μΩ-cm)
500	38.09	0.94	13.86
550	39.06	0.73	12.93
600	39.4	0.23	12.57
650	39.26	0.21	12.25

The thin film of Ru 40 nm on sapphire $(11\bar{2}0)$ deposited at 500°C has high resistivity and roughness, while the resistivity and roughness were decreased when increased the deposition temperature from 500°C to 650°C.

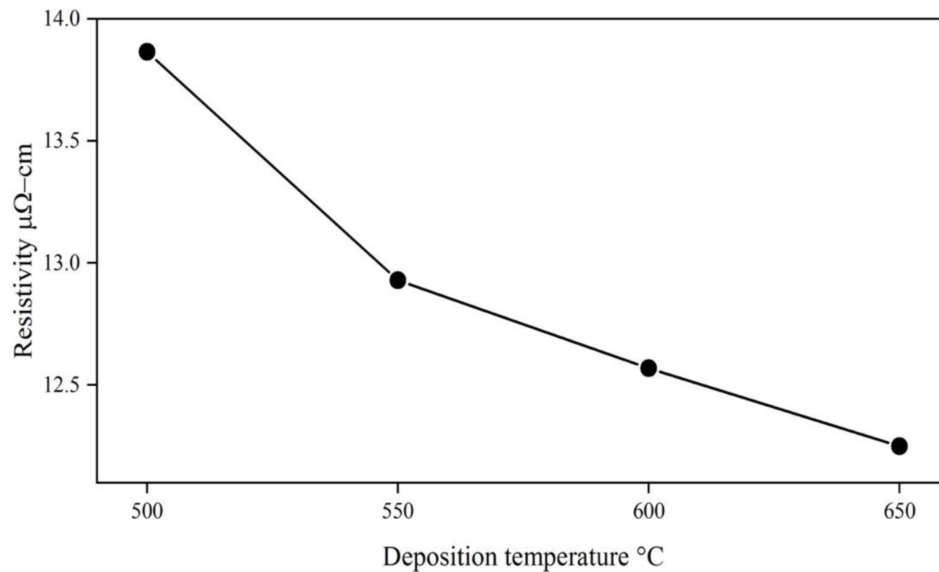

Figure 6-4 The resistivity of Ru 40 nm on sapphire $(11\bar{2}0)$

6.3 Ru on sapphire ($10\bar{1}0$)

Ru thin films were also deposited on ($10\bar{1}0$) oriented sapphire substrates at temperatures of 500°C, 550°C, 600°C, and 650°C, and these were not the desired Ru single crystal orientation, ($11\bar{2}0$) and were polycrystalline. These depositions used the same processing as in the Ru on sapphire ($11\bar{2}0$) described in section 6.1. The specular X-ray diffraction results from the sample deposited at 600°C from this series show a major peak at 68.2° from the ($10\bar{1}0$) sapphire substrate and peaks at 69.5°, 79.08°, and 84.7° for Ru ($11\bar{2}0$), ($10\bar{1}3$), and ($11\bar{2}2$) peaks, respectively. Figure 6-4 shows the 2θ specular scan for the Ru thin film on sapphire ($10\bar{1}0$).

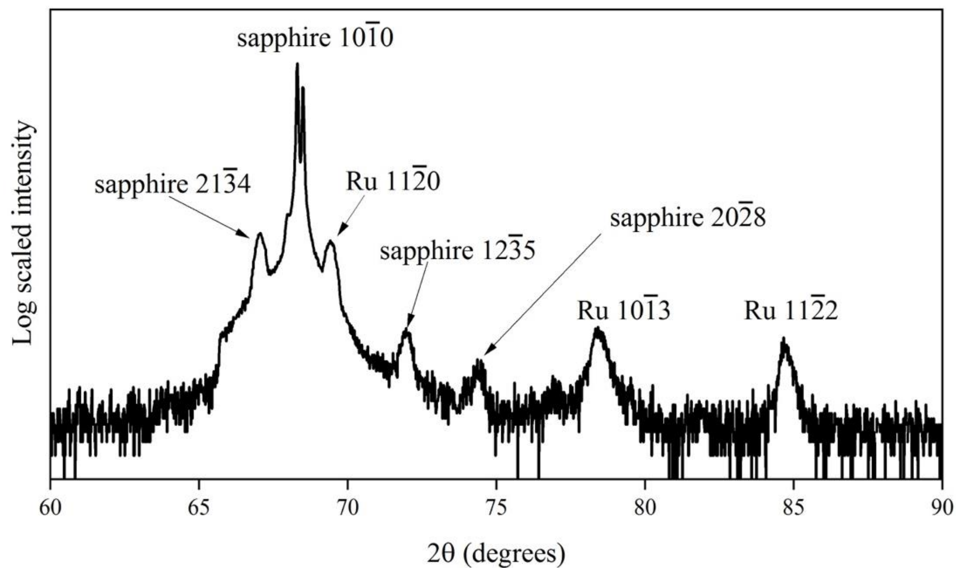

Figure 6-5 The 2θ scan of Ru thin film on sapphire ($10\bar{1}0$).

The resistivity of Ru 40 nm thin films was higher than Ru (0001) thin films on sapphire (0001) because these thin films were a polycrystalline. The data of these Ru thin films are in table 6-2.

Table 6-2 The thickness, roughness, and resistivity of Ru 40 nm thin films on sapphire $(10\bar{1}0)$.

Deposition temperature °C	Thickness (nm)	Roughness (nm)	Resistivity (μΩ-cm)
500	39.7753	1.27	13.01
550	39.1332	0.62	12.56
600	39.502	0.5	12.36
650	40.4996	0.48	12.07

The thin film of Ru 40 nm on sapphire $(10\bar{1}0)$ deposited at 500°C has low resistivity and roughness than the resistivity of Ru thin film on sapphire $(11\bar{2}0)$ deposited at 500°C. Where the resistivity and roughness were decreased also when increased the deposition temperature from 500°C to 650°C.

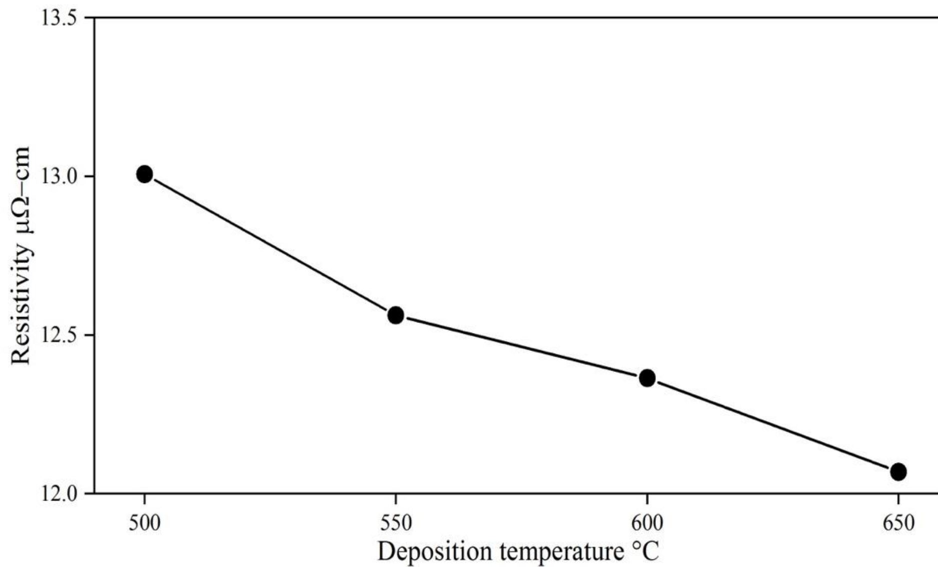

Figure 6-6 The resistivity of Ru 40 nm on sapphire $(10\bar{1}0)$

6.4 Ru on sapphire $(10\bar{1}2)$

Ru thin films were also deposited on $(10\bar{1}2)$ oriented sapphire substrates at temperatures of 500°C, 550°C, 600°C, and 650°C, and these were not the desired Ru single crystal orientation, were polycrystalline. These depositions used the same processing as in the Ru on sapphire $(11\bar{2}0)$ described in section 6.1. The specular X-ray diffraction results from the sample deposited at 600°C from this series show a major peaks at 25.56°, 52.53°, and 83.179° for the $(10\bar{1}2)$, $(20\bar{2}4)$, and $(30\bar{3}6)$ sapphire substrate and peaks at 42.402°, 69.5°, and 84.7° for Ru (0002), $(11\bar{2}0)$, and $(11\bar{2}2)$ peaks, respectively. Figure 6-4 shows the 2θ specular scan for the Ru thin film on sapphire $(10\bar{1}2)$.

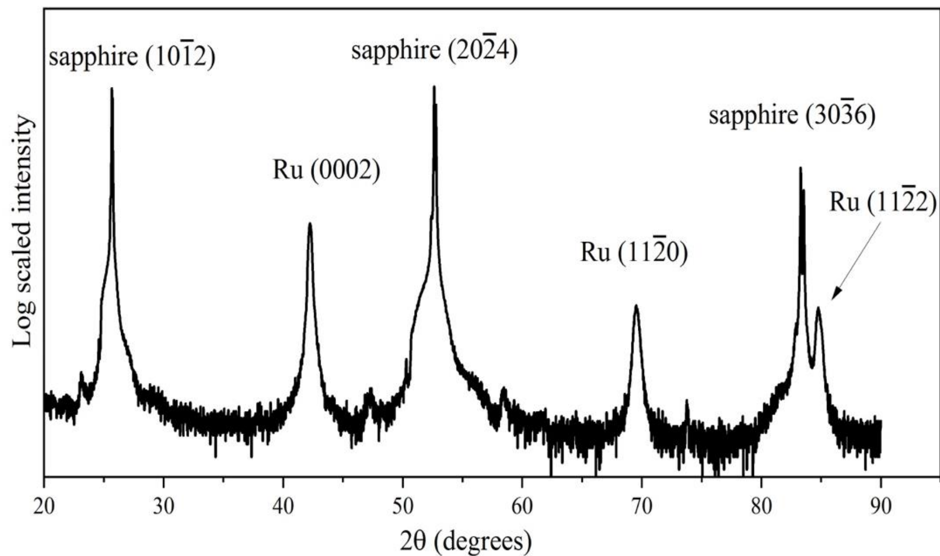

Figure 6-7 The 2θ scan of Ru thin film on sapphire $(10\bar{1}2)$

Table 6-3 The thickness, roughness, and resistivity of the Ru 40 nm thin films on sapphire ($10\bar{1}2$).

Deposition temperature °C	Thickness (nm)	Roughness (nm)	Resistivity (μΩ-cm)
500	39.17	0.98	12.50
550	39.33	0.72	11.46
600	39.62	0.57	11.21
650	39.21	0.39	10.25

The resistivity and roughness were decreased also when increased the deposition temperature from 500°C to 650°C.

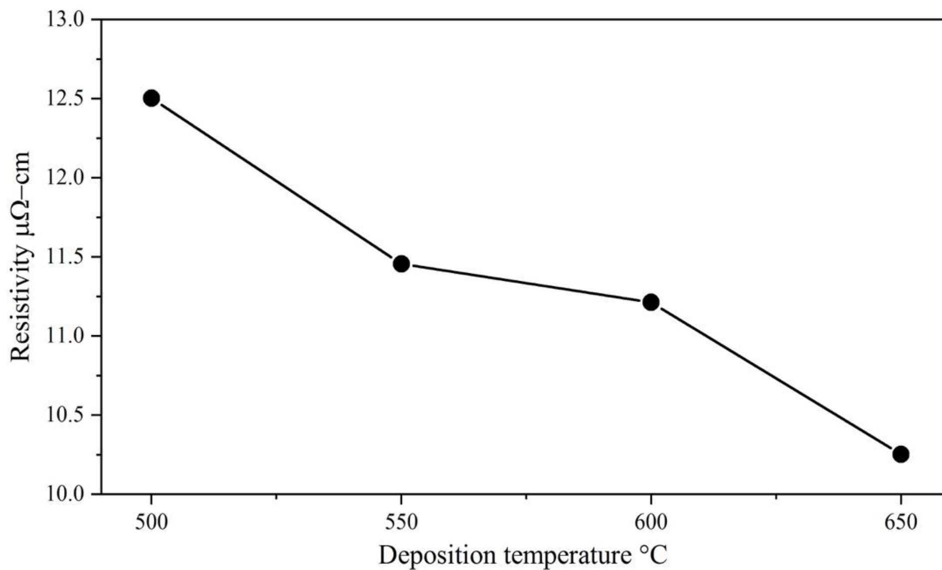

Figure 6-8 The resistivity of Ru 40 nm on sapphire ($10\bar{1}2$)

6.5 Ru on sapphire ($10\bar{1}4$)

The last depositions used the same processing as in the Ru on sapphire ($11\bar{2}0$) described in section 6.1. Ru thin films were deposited on ($10\bar{1}4$) oriented sapphire substrates at temperatures of 500°C, 550°C, 600°C, and 650°C, The specular X-ray diffraction results from the sample deposited at 600°C from this series show a major peaks at 35.139°, and 74.275° for the ($10\bar{1}4$),

and $(20\bar{2}8)$, sapphire substrate and peaks at 42.402°, and 92.093° for Ru (0002), and (0004) peaks, respectively. Figure 6-9 shows the 2θ specular scan for the Ru thin film on sapphire $(10\bar{1}4)$

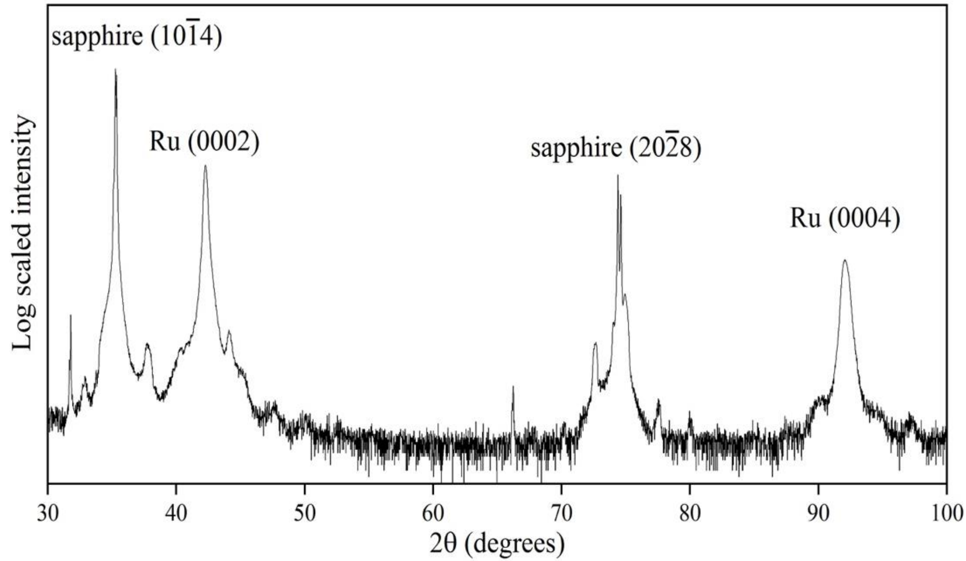

Figure 6-9 The 2θ scan of Ru thin film on sapphire $(10\bar{1}4)$

The resistivity of Ru thin films was higher than the other Ru thin films on $(11\bar{2}0)$, $(10\bar{1}0)$, and $(10\bar{1}2)$ sapphire substrates, even the Ru thin film that deposited at 650°C.

Table 6-4 The thickness, roughness, and resistivity of Ru 40 nm thin films on sapphire $(10\bar{1}4)$.

Deposition temperature °C	Thickness (nm)	Roughness (nm)	Resistivity (μΩ-cm)
500	39.14	0.95	15.73
550	39.42	0.71	15.61
600	39.81	0.63	15.25
650	39.28	0.44	13.98

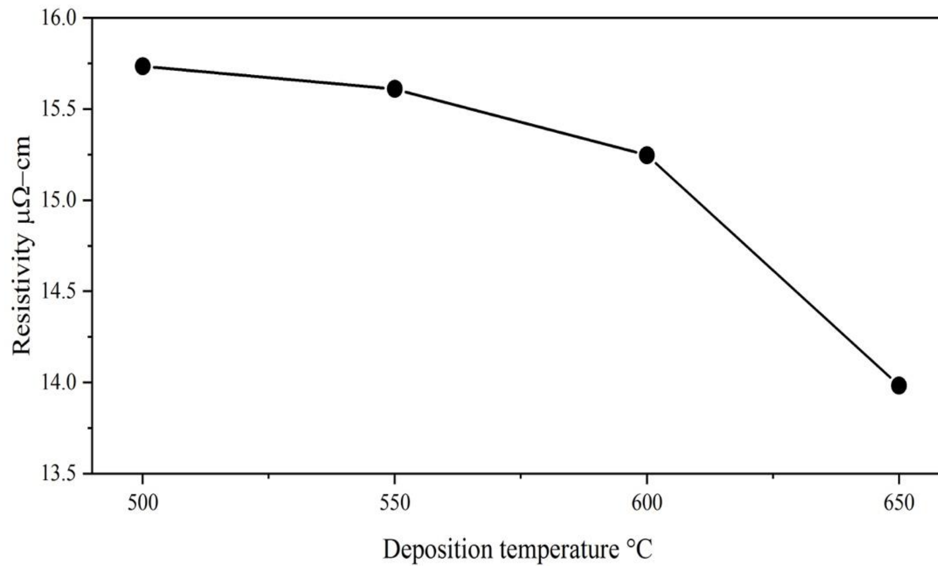

Figure 6-10 The resistivity of Ru 40 nm on sapphire ($10\bar{1}4$)

6.6 Conclusion

The single crystal of Ru has been grown on ($11\bar{2}0$), ($10\bar{1}0$), ($10\bar{1}2$), and ($10\bar{1}4$) sapphire substrates, Ru (0002) and Ru (0004) peaks have been grown on all sapphire substrates which Ru always prefer to grow on c-axis perpendicular to the sapphire. These attempts were unsuccessful for samples introduction and operated with a base vacuum in the low 10^{-8} Torr range and temperature (550°C, 550°C, 600°C, and 650°C).

CHAPTER 7 SUMMARY

Ru thin films on c-plane sapphire substrates have been grown by sputter deposition. The films were found to be epitaxial with a 30° offset in the phi positions of these peaks observed, as expected for the 30° rotational honeycomb epitaxial relationship of (0001) Ru || (0001) sapphire and $<11\bar{2}0>$Ru ||$<10\bar{1}0>$ sapphire. The resistivity of the Ru thin films showed dependence on processing, where the samples annealed at 700°C in Ar + H_2 3% (series 1) had higher resistivity than the samples that annealed at 950°C Ar + H_2 3% (series 2 and 3). The Ru surface roughness decreased after annealing in both cases. The resistivity versus thickness trends of sample series two and three are similar and can be described with a single set of FS model parameters. Using the same EMFP of 6.7 nm, the least squares fitting of the combined data for series two and three resulted in FS model parameters of ρ_o = 8.0 μΩ-cm and p = 0% (fully diffuse surface scattering). Alternatively, the data can be equally well by a EMFP of 11 nm and p = 39% (mostly specular surface scattering) with the same ρ_o = 8.0 μΩ-cm. This is shown as the solid line in Figure 4-6 for comparison to the experimental data. This thick film resistivity (ρ_o) is intermediate to that reported for a-plane resistivities of 7.5 and 8.2 μΩ-cm in bulk single crystal Ru samples

The deposition of SiO_2 on this surface, by sputtering or evaporation, was found to increase the resistivity and reduce the specularity of the surface. A subsequent anneal at 500°C in Ar + H_2 3% was found to restore the low resistivity and high specularity of the upper surface. Subsequent oxidizing anneals at 500°C and 400°C were again found to reduce the specularity of the upper surface while intermediate Ar + H_2 3% anneals were found to restore it. For the 20 nm thick Ru (0001) single crystal films, the relatively low and high specular scattering probabilities for the

upper Ru surface were found to differ in magnitude by approximately 60% and to be substantially reversible.

The deposition of Al_2O_3 on the Ru 20nm surface, by sputtering, was found to also increase the resistivity and reduce the specularity of the surface as a SiO_2. A subsequent anneal at 500°C in Ar + H_2 3% was found to restore the low resistivity and high specularity of the upper surface. Subsequent oxidizing anneals at 500°C was again found to reduce the specularity of the upper surface while intermediate Ar + H_2 3% anneals were found to restore some, where the resistivity was still higher than the Ru/SiO_2 after annealed at 950°C in Ar + H_2 3%.

The observation of surface specularity (sample series 3) greater than 60% is novel for a film surface not in UHV conditions. That this observation occurred for a buried metal/dielectric interface is a very significant and promising development for microelectronics, wherein all the interconnect wires are encased in dielectric and the surface scattering of these fully diffuse wire surfaces is currently limiting microprocessor speeds and consuming a majority of the electrical power.

CHAPTER 8 FUTURE WORK

8.1 Deposit Ru thin film on sapphire $(11\bar{2}0)$ and sapphire $(10\bar{1}0)$

Ruthenium has a hexagonal close-packed (hcp) crystal structure and even in bulk form has a lower electrical resistivity for current directed parallel to the crystallographic c-axis than for current in directions perpendicular to the c-axis. Of specific interest is that crystallographic planes perpendicular to the c-axis have lower surface energy and the electric current flowing parallel to the c-axis has lower resistivity The prior work allowed the formation of single crystal Ru films with the c-axis perpendicular to the film layer, which resulted in only the higher bulk resistivity directions available for nanowire semiconductor interconnects. The structure that was attempted to grow is a single crystal Ru film on an insulating substrate that has the c-axis in the plane, this will allow a significant reduction in the resistance of Ru when used for semiconductor interconnect nanowires.

The first attempts to deposit Ru thin film on other sapphire orientations to obtain Ru on an insulating substrate that has the c-axis in the plane was unsuccessful, as shown in chapter 6. Growing Ru c-axis in the plane may needs improved ultra-high vacuum or higher substrate temperaturea and is an important development for the future.

8.2 Ru (0001)/Metal oxide interfaces

The success of this research in obtaining reduced surface scattering of (0001) Ru/dielectric interfaces may be extended by the study of (0001) Ru/dielectric interfaces wherein the dielectric is crystalline, not amporhpous, and the interface is epitaxial. Studies of the interfaces of Ru

(0001) and metal oxide such as Cr_2O_3 or MgO will allow us to further understand the interfaces of these metal oxides with buried Ru (0001) surface.

8.3 The effect of annealing temperature

The annealing temperature for two hours at 500°C in Ar + H_2 3% or step anneals at 950°C in Ar + H_2 3% have a good effect to restore the low resistivity and high specularity of the upper surface of Ru, Ru/SiO_2 and Ru/Al_2O_3 films. Additional study of lower annealing temperatures decreased annealing time are of interest to avoid damage to semiconductor devices that may be present in applications.

LIST OF REFERENCES

1- Mishra, A.K., and Mishra, L., Ruthenium chemistry, Pan Stanford, **2018**.

2- Callister, W. D., Rethwisch, D. G., Materials science and engineering: an introduction, John Wiley & Sons New York, **2007**, Vol.7.

3- Pizzini, S and Rossi, L., Thermodynamics of the system ruthenium—oxygen. determination of the free energy of formation of RuO_2 by means of emf measurements, Z.Naturforsch, **1971**, 26a, 177.

4- Reed, T. B., Free energy of formation of binary compounds, MIT press, **1971**.

5- Livingstone S. E., The chemistry of Ruthenium, Rhodium, Palladium, Osmium, Iridium and Platinum, Pergamon press, **1973**.

6- Over H., Chem. Rev. **2012**, 112, 3356.

7- Wintterlin, J.,Trost, J., Renisch, S., Schuster, R., Zambelli, T., and Ertl, G., Real-time STM observations of atomic equilibrium fluctuations in an adsorbate system: O/Ru (0001), Surface science, **1997**, 394, 159.

8- Corriol C., Calleja F., Arnau A., Hinarejos J. J., Va´zquez de Parga A. L., Hofer W. A., Miranda R., Chemical Physics Letters, **2005**, 405, 131.

9- Kostov K. L., Gsell M., Jakob P., Moritz T., Widdra W., Menzel D., Surf. Sci. **1997**, 394, L138.

10- Stampfl C., Schwegmann S., Over H., Scheffler M., Ertl G., Phys. Rev. Lett. **1996**, 77, 3371.

11- Kostov K.L., Gsell M., Jakob P., Moritz T., Widdra W., and Menzel D., Observation of a novel high density 3O (2x2) structure on Ru (001), Surface science, **1997**, 394, L138.

12- Mitchell W.J., Xie J., Lyons K. J., Weinberg W. H., Dissociative chemisorption of oxygen on the Ru (001) surface: Spectroscopic identification of precursor intermediates at low surface temperatures, JVST A- Vacuum, Surfaces, and Films, **1994**, 12, 2250.

13- Mitchell W.J. Weinberg W H., Interaction of NO2 with Ru (001): Formation and decomposition of RuO x layers, The Journal of chemical physics, **1996**, 104, 9127.

14- He P., and Jacobi K., Vibrational analysis of the 1x1-O overlayer on Ru (0001)}, Physical Review, B, **1997**, 55, 4751.

15- Rahman T.S., Anton A.B., Avery N.R., and Weinberg W.H., Electron-energy-loss spectroscopy of ordered oxygen overlayers on Ru (001), Physical review letters, **1983**, 51, 1979.

16- Kim Y. D., Seitsonen A. P., Wendt S., Wang J., Fan C., Jacobi K., Over H., Ertl G., Phys. Chem. B, **2001**, 105, 3752.

17- Stampfl C., Surface processes and phase transitions from ab initio atomistic thermodynamics and statistical mechanics, Catalysis today, **2005**, 105, 17.

18- Over, H., Kim, Y. D., and Seitsonen A. P., Wendt, S., Lundgren E., Schmid M., Varga, P., Morgante A., and Ertl G., Atomic-scale structure and catalytic reactivity of the RuO2 (110) surface, Science, **2000**, 287, 1474.

19- Kim, Y. D., Schwegmann, S., Seitsonen, A. P., and Over, H., Epitaxial growth of RuO2 (100) on Ru (1010): Surface structure and other properties, J. Phys Chem., B, **2001**, 105, 2205.

20- Lin W. F., Zei M. S., and Kim, Y. D., Over H., and Ertl, G., Electrochemical versus gas-phase oxidation of Ru single-crystal surfaces, J. Phys Chem, B, **2000**, 104, 6040.

21- He Y.B., Knapp M., Lundgren E., and Over H., Ru (0001) model catalyst under oxidizing and reducing reaction conditions: in-situ high-pressure surface X-ray diffraction study, J Phys Chem, B, **2005**, 109, 21825.

22- Over H., Knapp M., Lundgren E., Seitsonen A. P., Schmid M., and Varga P., Visualization of atomic processes on ruthenium dioxide using scanning tunneling microscopy, ChemPhysChem, **2004**, 5, 167.

23- Wang J.X., Marinkovic N.S., Zajonz H., Ocko B.M., Adzic R.R., In situ X-ray reflectivity and voltammetry study of Ru (0001) surface oxidation in electrolyte solutions, J Phys chem., B, **2001**, 105, 2809.

24- Flege J. I., and Sutter P., Nanoscale analysis of Ru (0001) oxidation using low-energy and photoemission electron microscopy, j. Physics: Condensed Matter, **2009**, 21, 314018.

25- Blume R., et al., Catalytically active states of Ru (0001) catalyst in CO oxidation reaction, J. Catal. **2006**, 239, 345.

26- Blume, R., et al., Oxidation of methanol on Ru catalyst: Effect of the reagents partial pressures on the catalyst oxidation state and selectivity, Catalysis today, **2007**, 124, 71.

27- Wißmann P, in Surface physics, edited by G. Hohler, Springer Tracts in Modren Physics (Springer, New York, 1975).

28- Suhrmann R., Schulz K., Determination of the electronic interaction between adsorbed foreign molecules and the surface of thin nickel layers at low temperatures by electrical resistance measurements, Z. Phys chem. **1954**, 1, 69

29- K. Fuchs, The conductivity of thin metallic films according to the electron theory of metals, Proc. Cambridge Philos. Soc., **1938**, 34, 100.

30- E. H. Sondheimer, The mean free path of electrons in metals, Adv. Phys., **1952**, 1, 1.

31- A. F. Mayadas and M. Shatzkes, Phys. Rev. B 1, **1970**, 1382.

32- T. Sun, B. Yao, A. P. Warren, K. Barmak, M. F. Toney, R. E. Peale, and K. R. Coffey, Phys. Rev. B, **2010**, 81, 155454.

33- J. J. Thomson, Proc. Cambridge Philos. **1901**, Soc. 11, 120.

34- Chen F., and Gardner D., Influence of line dimensions on the resistance of Cu interconnections, IEEE Electron Device Letters, **1998**, 19, 508.

35- Semiconductor Industry Association and others, http://www. itrs. net, International Technology Roadmap for Semiconductors **2015** Edition.

36- Bietsch A., and Michel B., Size and grain-boundary effects of a gold nanowire measured by conducting atomic force microscopy, Applied physics letters, **2002**, 80, 3346.

37- Durkan C., and Welland M.E., Size effects in the electrical resistivity of polycrystalline nanowires, Physical review B, **2000**, 61, 14215.

38- Namba Y., Resistivity and temperature coefficient of thin metal films with rough surface Jap. J. Appl. Phys. **1970**, 9, 1326.

39- Rossnagel S. M., Kuan T. S., Alteration of Cu conductivity in the size effect regime, J. Vac. Sci. Technol. B, **2004**, 22, 240.

40- Marom H., and Eizenberg M., The effect of surface roughness on the resistivity increase in nanometric dimensions Appl. Phys. **2006**, 99, 123705.

41- Gall D., Electron mean free path in elemental metals, Appl. Phys., **2016**, 119, 085101.

42- Chawla J. S., and Gall D., Epitaxial Ag (001) grown on MgO (001) and TiN (001): Twinning, surface morphology, and electron surface scattering, Appl. Phys. **2012**, 111, 043708.

43- Zheng P. Y., Deng R. P., and Gall D., Ni doping on Cu surfaces: Reduced copper resistivity, Appl. Phys. Lett., **2014**, 105, 131603.

44- Zheng P., Zhou T., and Gall D., Electron channeling in TiO2 coated Cu layers, Semicond. Sci. Technol. **2016**, 31, 055005.

45- Dutta, S. et al, Highly scaled ruthenium interconnects, IEEE Electron Device Letters, **2017**, 38, 949.

46- Schumacher D., Surface scattering experiments with conduction electrons, Springer, **1993**, 128.

47- Chawla J. S., and Gall D., Specular Electron Scattering at Single-Crystal Cu (001) Surfaces, Appl. Phys. Lett., **2009**, 94, 252101.

48- Christmann K., Schober O., Ertl G., and Neumann M., Adsorption of hydrogen on nickel single crystal surfaces, J. Chem. Phys., **1974**, 60, 4528.

49- Watanabe M., and Hiratuka A., Reflection of light from gas adsorbed thin metallic films and their electrical resistance, Surface Science, **1979**, 86, 398.

50- Schmiedl E., Watanabe M., Wißmann P., and Wittmann E., The effect of gas adsorption on the electrical resistivity of thin silver films, Appl. Phys. A, **1984**, 35, 13.

51- Iwasaki Y., Izumi A., Tsurumaki H., Oizumi H., and Nishiyama I., Oxidation and reduction of thin Ru films by gas plasma, Appl. Surface Sci., **2007**, 253, 8699.

52- Hoffmann F. H., Weisel M. D., and Paul J., The activation of CO_2 by potassium-promoted Ru (001) I. FT-IRAS and TDMS study of oxalate and carbonate intermediates, Surface science, **1994**, 316, 277.

53- Herron J. A., Tonelli S., and Mavrikakis M., Atomic and molecular adsorption on Ru (0001), Surface science, **2013**, 614, 64.

54- Christmann K., Schober O., and Ertl G., Adsorption of CO on a Ni (111) surface, J. Chem. Phys, **1974**, 60, 4719.

55- Rauh M., Heping B., and Wißmann P., The effect of CO adsorption on the resistivity of thin Pd films, Appl. Phys. A, **1995**, 61, 587.

56- McCullen E. F., Hsu C., and Tobin R. G., Electron density changes and the surface resistivity of thin metal films: oxygen on Cu (100), Surface Science, **2001**, 481, 198.

57- Lin K. C., and Tobin R. G., Adsorbate-induced changes in the infrared reflectance and resistivity of metals, Phys. Rev. B, **1993**, 48, 2791.

58- Luo E. Z., Heun S., Kennedy M., Wollschläger J., and Henzler M., Surface roughness and conductivity of thin Ag films, Phys. Rev. B, **1994**, 49, 4858.

59- Persson B.N.J., Schumacher D., and Otto A., Surface resistivity and vibrational damping in adsorbed layers, Chem. Phys. Lett., **1991**,178, 204.

60- Persson B.N.J., Surface resistivity and vibrational damping in adsorbed layers, Phys. Rev. B, **1991**, 44, 3277.

61- Hein M., and Schumacher D., Changes of the DC resistivity and the broadband IR reflectivity of thin metal films due to coverage, J. Phys. D: Appl. Phys., **1995**, 28, 1937.

62- Jacob U., Vancea J., and Hoffmann H., Surface-roughness contributions to the electrical resistivity of polycrystalline metal films, Phys. Rev. B, **1990**, 41, 11852.

63- Krastev E. T., Kuhl D. E., and Tobin R. G., Multiple mechanisms for adsorbate-induced resistivity: oxygen and formate on Cu (100), Surface science, **1997**, 387, L1051.

64- P. Wißmann, The effect of gas adsorption on the conductivity of thin metal films, Thin Solid Film, **1972**, 13, 189.

65- Finzel H.-U., Schmiedl E., and Wiβmann P., The effect of surface roughness on the resistivity increase of thin metal films during gas adsorption, Appl. Phys. A, **1987**, 42, 87.

66- Watanabe M., and Wißmann P., Dielectric constants of adsorbed CO on Cu and Ag, Surface Science, **1984**, 138, 95.

67- X. Zhang, et al, Ruthenium interconnect resistivity and reliability at 48 nm pitch, IEEE Int. Interconnect Technol. Conf. / Adv. Met. Conf., **2016**, 31.

68- Dutta S.,Moors K., Vandemaele M., Adelmann C., Finite size effects in highly scaled ruthenium interconnects, IEEE Electron Device Letters, **2018**, 39, 268.

69- X. Zhang, et al, Methods to lower the resistivity of ruthenium interconnects at 7 nm node and beyond, IEEE International Interconnect Technology Conference (IITC), **2017**, 1.

70- Fan S.S.-C., Chen J.H.-C., Kamineni V.K., Zhang X., Raymond M., and Labelle C., IEEE Int. Interconnect Technol. Conf., **2017**.

71- Milosevic E., Kerdsongpanya S., Zangiabadi A., Barmak K., Coffey K. R., and Gall D., Resistivity size effect in epitaxial Ru (0001) layers, J. Appl. Phys. **2018**, 124, 165105.

72- D. Löffler D., et al, Growth and structure of crystalline silica sheet on Ru (0001)

Phys. Rev. Lett., 2010, 105, 146104.

73- Emmez E., Yang B., Shaikhutdinov S., and Freund H., Permeation of a single-layer SiO_2 membrane and chemistry in confined space, J. Phys. Chem. C, **2014**, 118, 29034.

74- B. Yang, et al, Thin silica films on Ru (0001): monolayer, bilayer and three-dimensional networks of [SiO_4] tetrahedra Phys. Chem. Chem. Phys., **2012**, 14, 11344.

75- C. Büchner, et al, Ultrathin silica films: The atomic structure of two-dimensional crystals and glasses, Chem. Eur. J., **2014**, 20, 9176.

76- Wu Y., Garfunkel E., and Madey T. E., Growth of ultrathin crystalline Al_2O_3 films on Ru (0001) and Re (0001) surfaces, Journal of Vacuum Science Technology A: Vacuum, Surfaces, and Films, **1996**, 14, 2554

77- Mubarak, A., Hamzah E., and Toff M., Review of Physical Vapour Deposition (PVD) Techniques for Hard Coating. Journal Mekanikal, **2005**. 20, 42-51.

78- Rossnagel, S., Thin Film Deposition with Physical Vapor Deposition and Related Technologies. J. Vac. Sci. Technol. A, **2003**, 21(5), S74.

79- http://lns00.psi.ch/sinqwiki/attach?page=VendorsManuals%2F2182A-900-01A.pdf

80- http://www.tek.com/sites/tek.com/files/media/document/resources/S530_VanDerPauwSheetRstnce.pdf

81- https://engineering.purdue.edu/Powerlab/Standard%20Operating%20Procedures/vFinal%20van%20der%20Pauw%20Testing%20User%20Guide%20%202014.pdf

82- Phi scan

83- J.M. Purswani, D. Gall, Electron scattering at single crystal Cu surfaces, Thin Solid Film. **2007**, 516, 465.

84- N. V. Volkenshtejn, V. A. Novoselov, V. E. Startsev, and E. P. Romanov, Anisotropy of the resistivity and hall coefficient of ruthenium in the low-temperature range, Metal. Metalloved., **1972**, 33, 105.

85- R.W. Powell, R. P. Tve, and M. J. Woodman, The thermal conductivity and electrical resistivity of polycrystalline metals of the platinum group and of single crystal of ruthenium, J. Less-common Metlas, **1967**, 12, 1.

86- J. T. Schriempf, and W. M. Macinnes, Electrical and thermal resistivities of ruthenium from 2 to 20K, Phys. Lett., **1970**, 33, 511.

87- C. Büchner, L. Lichtenstein, S. Stuckenholz, M. Heyde, F. Ringleb, M. Sterrer, W. E. Kaden, L. Giordano, G. Pacchioni, and H.-J. Freund, Adsorption of Au and Pd on ruthenium-supported bilayer silica, J Phys. Chem. C, **2014**, 118, 20959.

88- N. Akter, M. Wang, J.-Q. Zhong, Z. Liu, T. Kim, D. Lu, J. A. Boscoboinik, and D. J. Stacchiola, Stabilization of oxidized copper nanoclusters in confined spaces, Top Catal., **2018**, 61, 419.